Optimization and Hybridization of Membrane-Based Oxy-Combustion Power Plants

by

Surekha Gunasekaran

Bachelor of Technology, Indian Institute of Technology Madras (2011)

Submitted to the Department of Mechanical Engineering
in partial fulfillment of the requirements for the degree of

Master of Science in Mechanical Engineering

at the

MASSACHUSETTS INSTITUTE OF TECHNOLOGY

June 2013

Author .....
Department of Mechanical Engineering
May 10, 2013

Certified by .....
Alexander Mitsos
Visiting Scientist
Thesis Supervisor

Accepted by .....
David E. Hardt
Ralph E. and Eloise F. Cross Professor of Mechanical Engineering
Chairman, Department Committee on Graduate Theses

Optimization and Hybridization of Membrane-Based Oxy-Combustion Power Plants

by

Surekha Gunasekaran

Submitted to the Department of Mechanical Engineering
on May 10, 2013, in partial fulfillment of the
requirements for the degree of
Master of Science in Mechanical Engineering

Abstract

This thesis considers the optimization and hybridization of advanced zero emissions power (AZEP) cycles. More specifically, existing flowsheets for zero and partial emissions are optimized, and new integration schemes with solar energy are proposed and analyzed.

First, optimal design and operation of AZEP cycles, both zero and partial emissions, is considered. AZEP consists of a Brayton-like top cycle and a standard triple pressure heat recovery steam generator (HRSG) bottoming cycle, and a CO_2 separation and purification unit. The first-law efficiency is maximized as a function of CO_2 emissions with fixed ion transport membrane (ITM) size and consequently, variable power output. The optimization study involves 6 constraints, and 14 variables for the zero emissions cycle. The partial emissions cycle has one extra optimization variable. A two-step heuristic global optimization of the power cycle is performed. In the first step, the top cycle is optimized. In the next step, the bottoming cycle is optimized for fixed conditions of the top cycle. This procedure is repeated with different initial guesses for the optimization variables of the top cycle to obtain a near-global optimum. The optimization results in a significant increase in the efficiencies of AZEP100 and partial emissions cycles, in the range of 2-2.7 percentage points depending on cycle considered and ITM membrane temperature. This increase in efficiency is important with respect to viability of the partial emissions cycle compared to alternative power cycles. This viability is determined herein using a linear combination metric, which combines efficiency and CO_2 emissions. Optimization and simulations have shown that reducing the maximum membrane temperature results in an increase in the efficiency till membrane temperature reaches 850°C, after which the efficiency starts decreasing. However, reduced temperature results in dramatic drop in net power output of the power plant. In other words, membrane temperature results in a trade-off between power plant efficiency and power output.

Second, different solar-thermal integration schemes for an AZEP cycle with total CO_2 capture are proposed and analyzed. The solar subsystem consists of a parabolic trough, a Concentrated Solar Thermal (CST) technology. Four different integration schemes with

the bottoming cycle are considered: vaporization of high-pressure stream, preheating of high-pressure stream, heating of intermediate-pressure turbine inlet stream, and heating of low-pressure turbine inlet stream. The power outputs from these integration schemes are compared with each other and with the sum of the power outputs from corresponding stand-alone AZEP cycle and solar-thermal cycle. It is shown that vaporization of high-pressure stream in the bottoming cycle has the highest power output among the proposed integration schemes. The analysis shows that both the vaporization and heating of intermediate-pressure turbine inlet stream integration schemes have higher power output than the sum of the power outputs from corresponding stand-alone AZEP cycle and solar-thermal cycle. A comparison of the proposed vaporization scheme with existing hybrid technologies without carbon capture and sequestration (CCS) shows that it has a higher annual incremental solar efficiency than most hybrid technologies. Moreover, it has a higher solar share compared to hybrid technologies with higher incremental efficiency. Hence, AZEP cycles are a promising option to be considered for solar-thermal hybridization.

Thesis Supervisor: Alexander Mitsos
Title: Visiting Scientist

Acknowledgments

The work presented here in this thesis would not have been possible without the support of my family, friends, and colleagues. While it is impossible for me to thank everyone, I would like to thank a few people in particular. First and foremost, I want to thank my parents for all the support and inspiration they have given me. Secondly, I would like to thank my advisor for the time and effort he has put into helping me with my work. Thirdly, I want to thank my co-authors and colleagues for their insightful discussions which have benefited my work tremendously.

Finally, I would like to thank the King Fahd University of Petroleum and Minerals (KFUPM) in Dhahran, Saudi Arabia, for funding the research reported in this thesis through the Center for Clean Water and Energy at Massachusetts Institute of Technology (MIT) and KFUPM under project R2-CE-08. I also thank ASPEN Technology for providing access to ASPEN Plus®, and RES Group, Inc. for providing access to JACOBIAN® for this research. Further, I would like to thank Professors Esmail Mokheimer and Mohamed Habib for providing DNI data from the KFUPM weather station.

THIS PAGE INTENTIONALLY LEFT BLANK

Contents

THIS PAGE INTENTIONALLY LEFT BLANK

List of Figures

List of Tables

THIS PAGE INTENTIONALLY LEFT BLANK

Chapter 1

Advanced Zero Emissions Power Cycle

1.1 Introduction

Global warming and anthropogenic emissions of CO_2 have motivated the search for efficient and feasible environment-friendly technologies for power generation, which contributes to about 65% of total anthropogenic CO_2 emissions [5]. Carbon-dioxide capture and sequestration (CCS) allows for the use of fossil fuels for power generation without the detrimental effects of associated CO_2 emissions. There are various CO_2 capture techniques classified as pre-combustion, post-combustion and oxy-combustion [6]. First-law efficiency of almost all CCS plants are significantly lower than the conventional combined cycle plants without carbon capture. CCS plants typically incur a penalty of 7 to 11 percentage points [7] compared to conventional combined cycle power plants. The most conventional CCS technique is post-combustion capture, which requires energy-intensive and expensive CO_2 separation process [8]. Oxy-combustion provides a promising method that reduces the thermodynamic and economic penalty associated with the CO_2 separation process [9].

In oxy-combustion, O_2 is separated from air prior to the combustion of the fuel-air mixture and fuel oxidation occurs in a nitrogen-free environment, with large recirculation of exhaust

gases to control the temperature. The flue gas nominally consists only of CO_2 and H_2O, from which CO_2 can be separated relatively easily by condensation. Thus, the penalty associated with separation of CO_2 from the flue gas is greatly reduced [6]. Zebian et al. [10, 11] considered a pressurized oxycombustion process and demonstrated that simultaneous multivariable optimization of the entire process is required to obtain high performance; they also demonstrated that the process is ideally flexible to coal variations [12] and part-load [13]. At present, large-scale separation of O_2 from air is done using cryogenic air separation methods, which however, are energy intensive, or more precisely have low second-law efficiency [14]. A promising alternative is the use of ion transport membranes (ITM), which operate based on chemical potential differences, and use a high-temperature mixed-conducting (ionic and electronic) ceramic membrane [15]. This technology is motivated by the fact that the penalties incurred are much lower than the additional power requirement for cryogenic air separation [16].

1.2 Modeling

1.2.1 ITM Model

Oxygen separation in an ITM reactor consists of many complex physical processes which include bulk gas phase convective transport, ordinary and Knudsen molecular diffusion through porous structures, heterogeneous molecule-lattice kinetic interactions, and bulk ion diffusion through the crystal lattice [15, 17–21]. ITM technology requires thermodynamically strong integration schemes with the power plant to be competitive with cryogenic methods [20, 22]. Detailed computational fluid dynamics (CFD) studies require far too much computational time to capture the physical relationships between the state variables like temperature, pressure, etc. On the other hand, simplified black-box models cannot provide high-fidelity results, and therefore, cannot accurately predict interactions between different ITM operational and design parameters. Therefore, a reduced-order ITM model [23] is used here, which can capture the most significant physical processes without imposing an extreme

computational demand. A spatially-distributed quasi two-dimensional model implemented in JACOBIAN [24], based on fundamental conservation laws (mass and energy balance), semi-empirical oxygen transport equations, and fuel oxidation kinetics, is used in this work. Reference [23] gives a detailed description of this model.

1.2.2 ITM Oxy-Combustion Power Cycle Flow Sheet

Several ITM-based power cycles including advanced zero emissions power (AZEP) cycles [16, 25–29], ZEITMOP [30, 31], ITM-ATR [32] and ITM Oxy-coal [14] are described in the literature. Due to its high performance and compatibility, AZEP [8, 16, 20, 25–29] are the most commonly studied ITM-based power plant in the literature. The AZEP concept can be used for both (essentially) zero emissions cycles and partial emissions cycles. For partial emissions cycles, the base flow sheet is the same as the zero emissions cycle with the exception of the inclusion of an after-burner after the high-temperature heat exchanger ("HHEX") in order to increase the gas turbine inlet temperature to the maximum possible limit (herein assumed to be 1300°C), which increases the efficiency and also increases the CO_2 emissions. Zero emissions AZEP cycles are denoted as AZEP100, which imply 100% CO_2 capture, whereas various partial emissions variants are denoted as AZEPXX where XX denotes the percentage of CO_2 emissions captured, e.g., AZEP72, in which 72% of CO_2 emissions are captured. The focus of this article is optimization of both zero and partial emissions AZEP cycles. This section gives a brief summary of the modeling methodology of zero and partial emissions AZEP cycles adopted here, of which a detailed description is given in Reference [20].

AZEP can be seen as a combined cycle. The top cycle is a Brayton-like cycle with an ITM air separation unit and a combustor. Figure 1-1 shows the zero and partial emissions concept, where the additional fuel stream "AFTRMETH" and after-burner are not there for zero emissions cycle. The air is compressed and split into two streams -"AIRMCM" and "AIRREST". The feed stream to the ITM is preheated by the recycled combustion products with a heat exchanger network (see "LHEX-ITM-HHEX" shown in Figure 1-1).

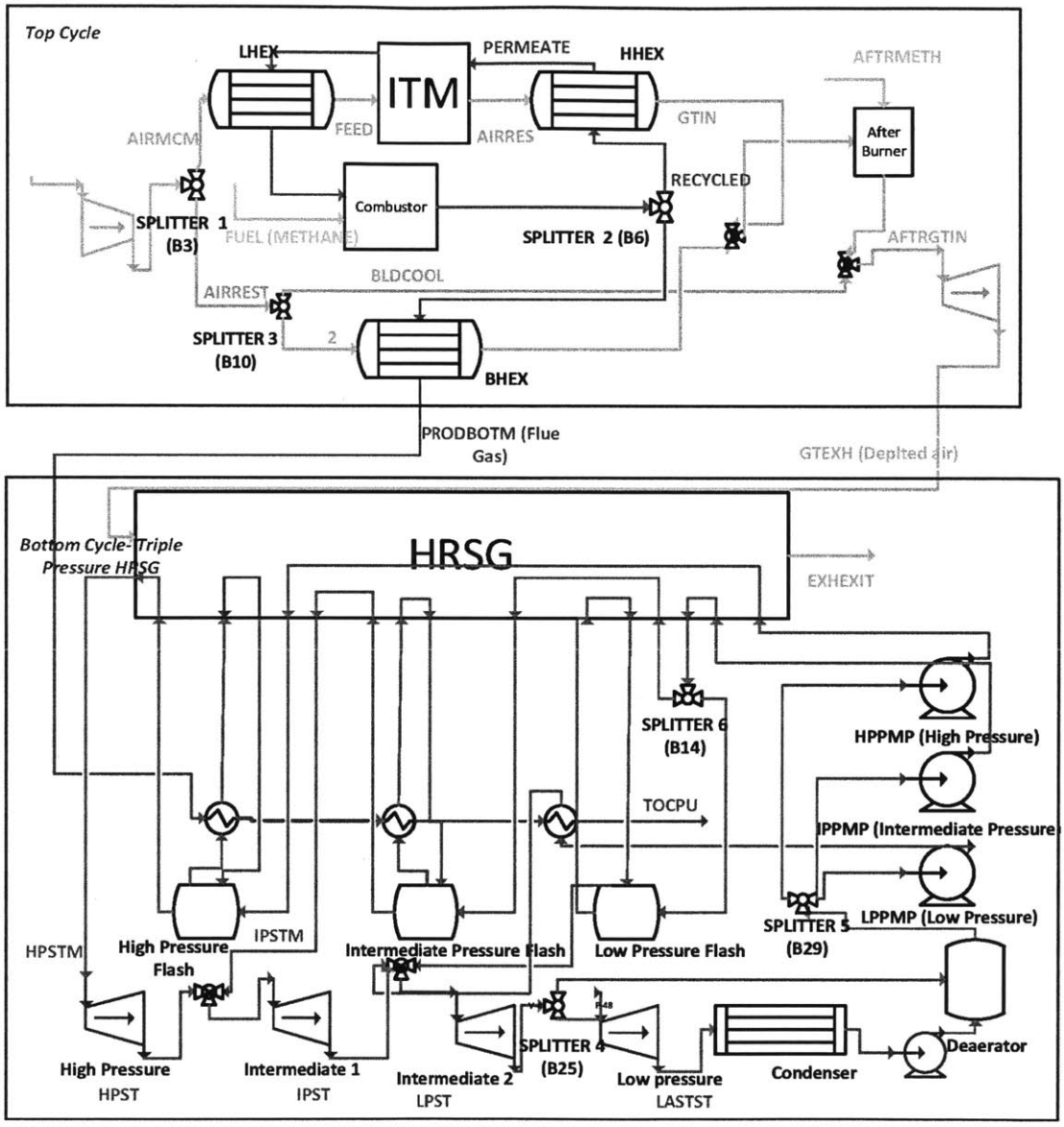

Figure 1-1: AZEP Cycle Process Flow Diagram in ASPEN Plus® with a JACOBIAN based ITM model. Bottoming cycle is triple pressure HRSG with pressure levels 100, 25, 5 bar. The stream "AFTRMETH" and the after-burner "AFTERBR" are omitted for the AZEP100.

"AIRMCM" is preheated to 700°C in the heat exchanger "LHEX". This preheated feed stream provides oxygen to the permeate stream in the ITM. The "AIRRES" exiting the ITM (O_2 depleted stream) is further heated by the combustion products "RECYCLED" (which serves as the permeate stream in the ITM) and is directly expanded in the gas turbine in case of zero emissions cycle. In case of partial emissions cycles "AIRRES" after getting heating by "RECYCLED" is combusted in the after-burner with the additional fuel stream "AFTRMETH" and then expanded through the gas turbine. This is done in order to increase the gas turbine inlet temperature and thus increase the first-law efficiency of the power plant.

The permeate stream contains O_2 (from the feed stream) necessary to burn the required amount of fuel. In both variants, fuel flow rate into the combustor is calculated such that stoichiometric combustion takes place. Stoichiometric combustion is optimal as there is no excess fuel or O_2 left-over in the flue gas. If some amount of oxygen is unconsumed, it means that excess ITM area (above what is necessary) is used, and results in more ITM pressure drop. Unconsumed O_2 also results in more work to separate CO_2 from the flue gas, which also contains O_2. On the other hand, if fuel remains unreacted, efficiency directly drops, and thus unit electricity cost increases. Moreover, unreacted fuel would also necessitate the need for a complex gas separation process to separate out CO_2 from the flue gas. A part of "AIRREST" is used to cool the gas turbine and a part is used to regenerate thermal energy from the combustion products in the heat exchanger "BHEX". As described in Section 2.2.1, it is advantageous to extract the maximum possible power from the gas turbine and transport less thermal energy to the bottoming cycle. Therefore, the air outlet temperature from the heat exchanger "BHEX" must be the maximum possible, while satisfying the pinch. Fixing the pinch which occurs at the hot end to 10°C, for inlet temperature of combustion products 1200°C, the outlet temperature of air must be 1190°C. Therefore, the outlet temperature of air from "BHEX" is fixed at 1190°C.

The temperature of combustion products is limited by the temperature limit of the high-temperature heat exchanger "HHEX". A design specification control loop is implemented

to maintain the temperature of the combustion products at 1200°C by varying the split fraction of the compressed air ("Splitter 1"). Another design specification control loop varies the recycle ratio (split fraction of "Splitter 2") to maintain a pinch of 10°C without any temperature cross over in the heat exchanger network "LHEX-ITM-HHEX". The amount of "GT" turbine blade cooling air required is chosen according to performance maps (Chart 5.16 of Reference [33]), and is implemented using a design specification. Performance maps specify the amount of blade cooling air required based on the turbine inlet temperature. From Chart 5.16 of Reference [33], the average of the lower and upper limits of this range is chosen for the present study. This leads to a flow rate of "BLDCOOL" (in kmol/h) that is proportional to the total air flow rate (in kmol/h) and a temperature-dependent term $3.4\times10^{-4}\times(T-1027)$, where T is the temperature of gas turbine inlet stream "AFTRGTIN" in °C.

A design specification is also implemented to not allow the turbine inlet temperature to exceed 1300°C. The "PRODBOTM" stream after extraction of thermal energy in "BHEX" and the "GTEXH" (outlet from the turbine) are fed to the bottoming cycle for extraction of work from the thermal energy of these streams. A standard triple pressure heat recovery steam generator (HRSG) cycle is used as the bottoming cycle for the zero emissions and partial emissions cycles (Figure 2-2). In the reference simulation without optimization of AZEP cycle for maximizing efficiency (described in Section 2.2), the three pressure levels of the triple pressure HRSG cycle are fixed at 100, 25 and 5 bars respectively. A design specification control loop is implemented to fix the pinch of HRSG to be 5°C in the reference simulation by varying the total steam flow rate. The outlet stream "TOCPU" is fed to the compression and purification unit (CPU) to separate H_2O and CO_2.

Chapter 2

Optimal Design and Operation of Membrane-Based Oxy-combustion Power Plants

2.1 Introduction

This chapter focuses on multi-variate optimization of AZEP cycle [16, 25–29] to study its viability. As shown by Mancini and Mitsos [20], most of the partial emissions cycles without optimization are not viable in the linear combination metric that they introduced, which combines CO_2 emissions and efficiency. A detailed description of the linear combination metric is given in Section 2.3.2. Optimization of the partial emissions power cycle is needed to assess its viability, compare also Zebian et al. [10]. In this work, for fixed ITM size, the first-law efficiency of the power cycle is maximized for various CO_2 emissions, which consequently results in variations of net power output. A two-step heuristic global optimization of the power cycle is performed. First, only the top cycle is optimized with a local solver. Then, the bottoming cycle is optimized, again with a local solver, using the inlet streams to the bottoming cycle fixed to the optimum operating condition of the top cycle. The two-step procedure is repeated with different initial guesses for the optimization variables of the top

cycle to obtain a near-global optimum. The optimization study involves 6 constraints, and 14 variables for the zero emissions cycle. The partial emissions cycle has an extra optimization variable. The importance of multi-variable optimization is demonstrated by the improvement in efficiency and change in the viability status. Optimization also demonstrates the effect of membrane temperature on efficiency, as well as a trade-off between efficiency and power output per unit membrane area.

2.2 Optimization of AZEP cycle

2.2.1 Motivation and Formulation

A heuristic global optimization is performed using the sequential quadratic programming solver available in ASPEN Plus®. The one-dimensional intermediate fidelity ITM model does not allow optimization of the ITM geometry. Attempting to minimize the pressure drop would result in an infinite number of permeate and feed channels, of infinitesimal length. Moreover, the ITM is an expensive component, so optimization of the ITM size would require accurate estimates for its cost which are not available since ITM is a very new technology. Therefore, for the purpose of our study, the area of the ITM is held constant at 400 m^2. Overall, the objective is maximal efficiency for various values of CO_2 emissions, which in turn results in variation in fuel flow rate and power output. The power cycle has 14/15 optimization variables for the zero/partial emissions AZEP cycle respectively – 6/7 variables for the top cycle of zero/partial emissions AZEP cycle respectively, and 8 for the bottoming cycle. Operational variables which are optimized are: mass flow rate of streams "AFTRMETH", "AIRREST", "AIRMCM", split fractions of "Splitter 2", "Splitter 3", "Splitter 4", "Splitter 5" ("LPFW" stream), "Splitter 5" ("LPIPFW" stream)", "Splitter 6". Design variables considered for optimization include: air outlet temperature of heat exchangers "LHEX" and "BHEX", the outlet pressure of condenser pump "CONDPUMP", and the pressure levels of the bottoming cycle which include outlet pressures of pumps "HPPMP", "IPPMP" and "LPPMP". Fuel flow rate to the after-burner, which is set to

zero in case of zero emissions cycle, is an additional optimization variable in case of partial emissions cycles. To overcome numerical difficulties and limitations of ASPEN Plus®, the power cycle is optimized in two steps. First, only the top cycle is optimized. Then, only the bottoming cycle is optimized using the inlet streams to the bottoming cycle - "GTEXH" and "PRODBOTM" - as input specifications, fixed to the optimum operating condition of the top cycle. In principle, this two-step method does not guarantee local optimization of the entire cycle [34]. However, as the efficiency of the top cycle is higher than that of the bottoming cycle, it is more efficient to extract work through the gas turbine in the top cycle than the bottoming cycle where power is produced using low temperature streams. In other words, to attain maximum efficiency of the total power plant, maximum possible power extraction should take place in the top cycle, transporting minimum thermal energy to the bottoming cycle. Thus, sequential optimization of the top cycle followed by the bottoming cycle is expected to give the optimum of the entire power cycle. As the work required for separation of CO_2 from the flue gas in the CPU is small (less than 2% of the net power), the compression and purification unit is not optimized. Since the SQP solver can not guarantee a global optimum, the two-step procedure is repeated with 50 different initial guesses for the optimization variables of the top cycle, and the best among them is assumed to be a near-global optimum and is reported here. Preliminary optimization results for the AZEP100 power cycle were presented at the 25th ECOS 2012 Conference held in Perugia [35]. Therein, partial emissions cycles were not optimized.

Optimizing the efficiency of top cycle of AZEP100

The optimization variables of the top cycle are: the mass flow rates of "AIRMCM" and "AIRREST", the split fraction of "Splitter 3" and "Splitter 2", and the cold-side outlet temperatures of heat exchangers "LHEX" and "BHEX". Varying "AIRMCM" varies fuel flow rate since flue flow rate is stoichiometrically related to the amount of O_2 separated in the ITM to ensure complete combustion (see Section 1.2.2). As the mass flow rate of "AIRMCM" increases, the amount of oxygen separated by a fixed-size ITM also increases.

This corresponds to an increase in fuel flow rate and greater compressor power (decrease in efficiency). At the same time, the power output from the turbine increases due to increase in mass flow rate (increase in efficiency). The combination of these opposing effects provides scope for optimization. As the mass flow rate of "AIRREST" increases, the compressor power and flow rate through the turbine increase, thus increasing the power output from the gas turbine the "GT". At the same time, increase in "AIRREST" flow rate, keeping the "Splitter 3" split fraction constant, decreases the input temperature to the turbine, which decreases the output power. A similar effect is seen for the variation of the "Splitter 3" split fraction. For fixed "AIRREST" flow rate, increased direct flow through the gas turbine results in lower gas turbine "GT" inlet temperatures. However, this results in smaller flow rates through "BHEX" and thus, the maximum energy in the heat exchanger is not extracted. Larger air-flow through "BHEX" is expected to produce more power in gas turbine "GT". Other factors such as a higher air compression power required, and lower air outlet temperature in "BHEX" also come into play. The outlet temperature of "LHEX" also plays an important role in determining ITM performance. Therefore, the interplay of these effects emphasizes the importance of optimization. Table 2.1 shows the results of optimization of top cycle with a maximum ITM temperature of 1000°C.

To facilitate convergence of the ASPEN Plus® optimizer, the design specifications of the top cycle (maximum combustion temperature of 1200°C, turbine blade cooling, and the pinch in the heat exchanger network "LHEX-ITM-HHEX" to be greater than 10°C) are implemented as optimization constraints. The split fractions of "Splitter 1", "Splitter 2" and "Splitter 3", which are treated as design specification variables in the reference simulations (without optimization), are treated as optimization variables. This means that design specifications now become optimization constraints, and in the process, design specification variables now become optimization variables. The air outlet temperature of "BHEX" is also treated as an optimization variable. The tolerance of all the constraints except turbine balde cooling is specified to be 1°C, and for turbine blade cooling it is specified to be 10 kmol/h. Figure 2-1 shows the optimization variable and constraints used in the top cycle.

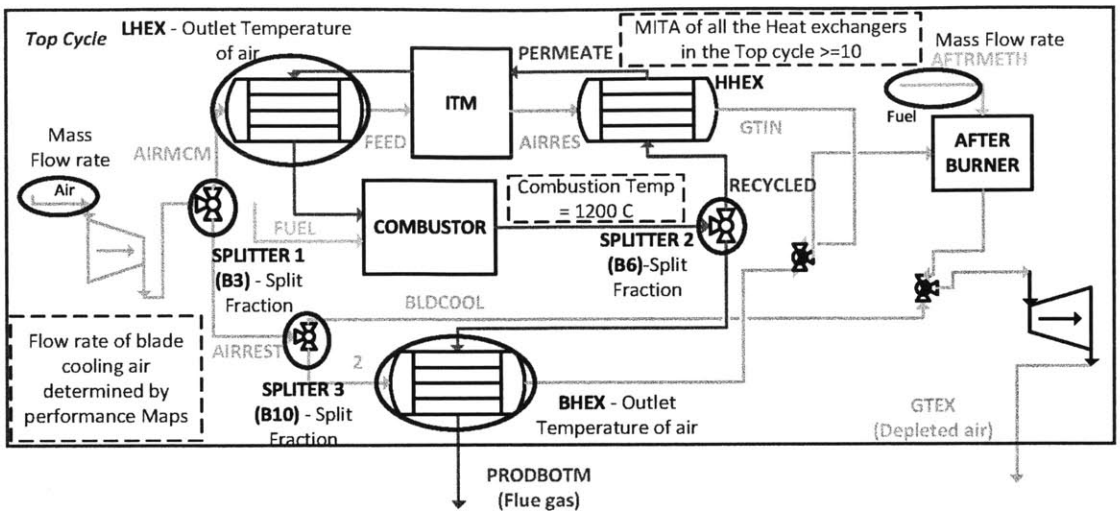

Figure 2-1: AZEP Top Cycle Process Flow Diagram with optimization variables circled, and constraints boxed in dashed black lines.

Optimization of Bottoming Cycle of AZEP100

The bottoming cycle is a triple pressure HRSG. The input specifications of the streams "GTEHX" and "PRODBOTM" are specified using the results obtained from the optimized top cycle, and the bottoming cycle is then independently optimized. The variables considered for optimization of the bottoming cycle include the three pressure levels, the discharge pressure of the turbine and the condenser pump, and the split fraction of the three splitters. Lowering the temperature of air stream "EXHEXIT" which exits the HRSG into the atmosphere, and increasing the temperature of streams "HPSTM" and "IPSTM" which exit the HRSG to be expanded by the turbines "HPST" and "IPST" respectively, increases the efficiency since the heat input to the bottoming cycle increases. Thus, the outlet temperature of the stream "EXHEXIT" is lowered, and that of the streams "HPSTM" and "IPSTM" is increased to the maximum possible extent, such that there are no temperature crossovers in any of the heat exchangers. These streams - "HPSTM" and "IPSTM" are the outlet streams from the HRSG expanded through the high pressure and medium pressure turbines. Increasing the temperature of these streams and decreasing the temperature of "EXHEXIT"

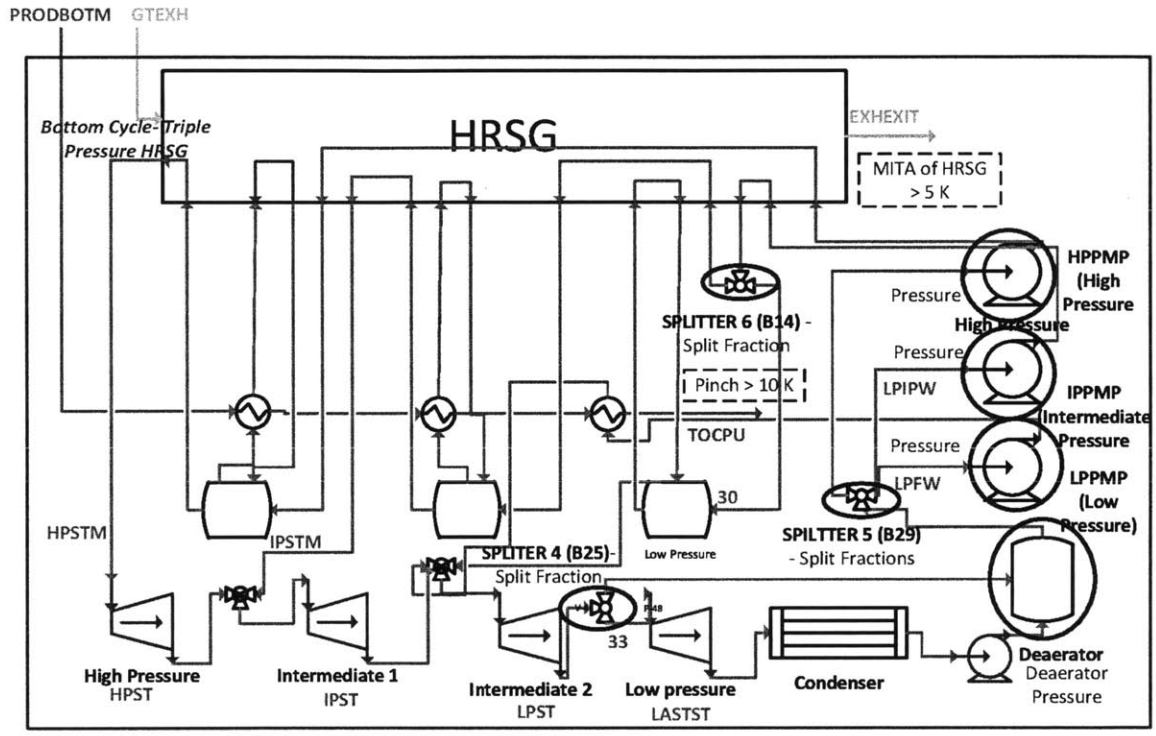

Figure 2-2: AZEP Bottoming Cycle Process Flow Diagram with optimization variables circled, and constraints boxed in dashed black lines.

imply increasing the heat input into the bottoming cycle, thus increasing the efficiency. The temperature of "EXHEXIT" can be reduced without any constraint for zero emissions and partial emissions cycles since the acid condensation temperature of stream "GTEXH" is approximately 30°C, which is much lower that the temperature stream "GTEXH" can reach without any temperature crossovers in HRSG.

The discharge pressure of "LASTST" is fixed to be equal to the saturation pressure at 25°C to maintain a 5°C temperature difference with the atmospheric temperature, which is assumed to be 20°C. Unlike the top cycle, implementing design specifications as optimization constraints does not work well for the bottoming cycle. It is found that implementing design specifications and optimization constraints as separate units for the bottoming cycle makes the optimizer convergence easier. The optimization constraints also include specifying the outlet stream from the de-aerator as saturated liquid. Figure 2-2 shows the optimization variables and constraints used in the bottoming cycle. For the design specification that specifies the pinch of HRSG to be greater than 5°C, the tolerance is fixed at 1°C, and for the optimization constraint that specifies the vapor fraction of outlet stream from the de-aerator, the tolerance is 0.01.

Optimization of Partial Emissions Cycles

The partial emissions cycles (AZEPXX) have an additional optimization variable in the top cycle which is the mass flow rate of additional fuel stream "AFTRMETH" subject to the constraint that turbine inlet temperature should not exceed 1300°C (assumed maximum due to material constraints). For maximum membrane temperature equal to 1000°C, AZEP72 partial emissions cycle is the result of 1300°C turbine inlet temperature. Other partial emissions cycles which have CO_2 capture rate between 100% and 72% are obtained by adding a constraint which specifies the ratio of fuel added in the combustor and after-burner. Results of AZEP72 partial emissions cycle and other partial emissions cycle are reported in the Appendix A.

Table 2.1: Results and Formulation of Optimization of Top Cycle (Membrane Temperature = 1000°C, CO_2 Capture = 100%)

Variables	Units	Before Optimization	After Optimization	Range
Molar Flow rate of AIRREST	kmol/s	5.67	7.81	[2.5-13.6]
Molar flow rate of AIRMCM	kmol/s	37.3	41.1	[15-55]
Split fraction of Split 2 (BLDPROP)		0.127	0.116	[.1-.2]
Split fraction of Split 3 (Stream2)		0.73	0.713	[.1-.9]
Air Outlet Temperature of LHEX	K	973	873	[823-988]
Air Outlet Temperature of BHEX	K	1463	1463	[1200-1500]
ITM ΔP_{Tot} feed/permeate (%)		1.1/0.6	1.18/7.73	
ITM Recovery ratio		29.1	30.8	
Efficiency contribution $\left(\frac{\text{Power output from top cycle}}{\text{Heating valuex Fuel Flow rate}}\right)$		25.3%	26.2%	

2.3 Results and Discussion

2.3.1 Optimization results of AZEP100 with membrane temperature = 1000°C

As seen from Table 2.1, the mass flow rates of both "AIRMCM" and "AIRREST" have increased. This implies greater power produced by the "GT" turbine. Split fraction of "Splitter 2" varies to attain minimum approach temperature in heat exchanger "LHEX" without any temperature crossover in the heat exchanger network "LHEX-ITM-HHEX" (implemented as one of the constraints). A decrease in air outlet temperature from the heat exchanger "LHEX" is seen for AZEP100. It is also seen that air outlet temperature from "BHEX" remains 1190°C as any further increase in air temperature would decrease the pinch which happens at the hot side below 10°C. The first-law efficiency contribution of the top cycle, which is defined as the ratio of power output to the product of heating value of the fuel and the fuel flow rate, increases by 0.9 percentage points (from 25.3% to 26.2%) as a result of the optimization.

Table 2.2 shows the results of optimization of the bottoming cycle. Optimization of the bottoming cycle increases its efficiency contribution (bottoming cycle efficiency contribution is defined as the ratio of power output from the bottoming cycle to the product of fuel flow

Table 2.2: Results and Formulation of Optimization of Bottoming cycle (Membrane Temperature = 1000°C, CO_2 Capture = 100%)

Variables	Units	Before Optimization	After Optimization	Range
Outlet Pressure of HPPMP	bar	100	98	[75-105]
Outlet Pressure of IPPMP	bar	25	26.2	[20-40]
Outlet Pressure of LPPMP	bar	5	4.39	[3-10]
Outlet Pressure of CONDPUMP	bar	0.2	0.20	[.15-.3]
Split fraction of Split 5 (LPFW)		0.14	0.199	[.1-.9]
Split fraction of Split 5 (LPIPFW)		0.083	0.197	[.08-.2]
Split fraction of Split 6 (Stream 30)		0.3	0.239	[.1-.4]
Split fraction of Split 4 (Stream 33)		0.95	0.94	[.8-1]
Outlet Temperature of air from HRSG (EXHEXIT)	K	400	383	
Outlet Temperature of steam from HRSG to HPST (HPSTM)	K	733	758	
Outlet Temperature of steam from HRSG to IPST (IPSTM)	K	733	758	
Efficiency contribution $\left(\frac{\text{Power output from bottoming cycle}}{\text{Heating valuex Fuel Flow rate}}\right)$		22.7%	23.4%	

Table 2.3: Summary of Optimization of Top and Bottoming cycle (Membrane Temperature = 1000°C, CO_2 Capture = 100%)

Efficiency contribution	Before Optimization	After Optimization	Increment in % points
Top Cycle	25.3%	26.2%	0.9
Bottoming Cycle	22.2%	23.4%	1.2
Power Plant	47.5%	49.6%	**2.1**

rate and heating value) from 22.2% to 23.4% (shown in Table 2.2). The total efficiency of the power plant thus increases by 2.1 percentage points. This is a significant improvement in the efficiency, which plays an important role in determining the feasibility of AZEP cycles, see also the discussion in the next section. A summary of results from the optimization of the top and bottoming cycles is shown in Table 2.3.

2.3.2 Assessment of partial emissions cycles

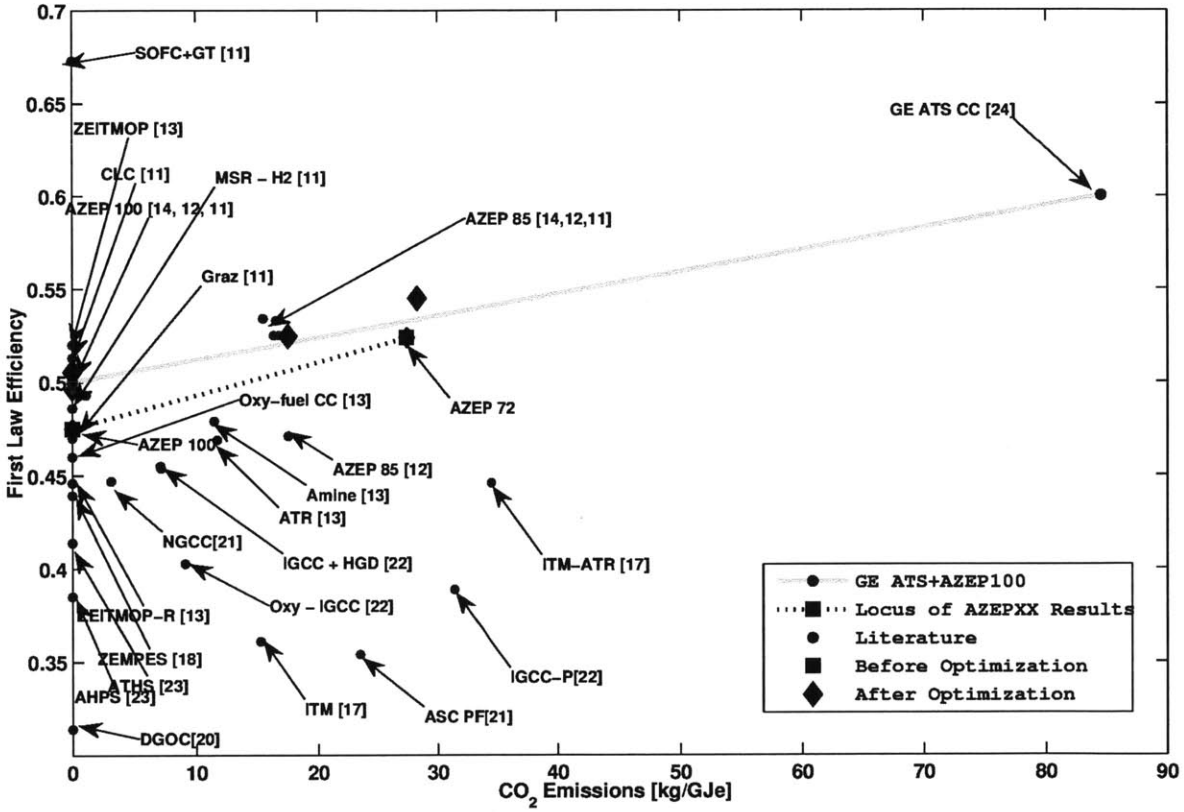

Figure 2-3: Assessment of partial emissions cycle for AZEPXX, ZEITMOP, AHPS, DGOC, ATHS, ITM-ATR, Oxy-fuel CC, Oxy-IGCC, Oxy-NGCC, variations of AZEP cycle before and after optimization.

Different variations of partial emissions ITM cycles have been proposed to increase efficiency. Improving the efficiency of a partial emissions cycle by a small fraction is not very useful if the CO_2 emissions simultaneously increases by a large amount. The simultaneous

increase in efficiency and CO_2 emissions makes the partial emissions cycle difficult to judge for viability. Mancini and Mitsos [20] proposed a new metric for multiple objectives (see Figure 2-3), which compares plants at the fleet level, and provides a good measure for judging the viability of partial emissions cycles. Note that Sheu et al. [36] gave a more thorough analysis of this metric applied to hybrid fossil-renewable plants. Figure 2-3 shows the first-law efficiency and specific CO_2 emissions for different cycles which have been studied in the literature [14, 16, 25–27, 30, 32, 37–44]. A linear combination of the AZEP100 cycle and a conventional combined cycle with no CCS technology is also shown for comparison in Figure 2-3. The black dotted line represents the stipulated locus of partial emissions cycles from AZEP100 to AZEP72 [20] without optimization. The solid line shows the efficiency and the specific CO_2 emissions for different combinations of the AZEP100 cycle and the most efficient combined cycle without carbon capture reported in the literature (60%). For a given CO_2 emissions, a partial emissions cycle is viable if it has higher efficiency than the combination of an AZEP100 and a combined cycle [20], i.e., if it lies above the solid line in Figure 2-3. Almost all partial emissions cycles proposed in the literature are seen to lie below the solid line, and are therefore not viable. Our optimized AZEP100 cycle and partial emissions cycles lie above the solid line, indicating that they are viable. Therefore, optimization studies are crucial for determining the feasibility of zero and partial emissions cycles. The efficiency of the partial emissions cycle after optimization is slightly higher than the corresponding point on the solid line. However, other factors such as the penalty for gas cleanup before letting the exhaust gas into the atmosphere not included in the model may bring down the efficiency of the partial emissions cycle. This may lead to comparable efficiencies for the partial emissions cycle and the combination of zero emissions and a conventional combined cycle with no CCS. Thus, for fixed CO_2 emissions, there exists a choice between the two that can be met using different criteria. In addition, it must be noted that fuel-cell based processes can achieve substantially higher performance, but require completely different technology.

2.3.3 Effect of membrane temperature on optimal efficiency

In order for the results reported above to be consistent with those reported by Mancini and Mitsos [20], the maximum allowed membrane temperature is set to 1000°C. This is implemented by controlling the temperature of stream "PERMEATE" from the heat exchanger "HHEX". Since the temperature of "FEED" entering the ITM is around 700°C and the ITM is assumed to be adiabatic, the temperature of the "PERMEATE" stream is equal to the maximum membrane temperature. The maximum allowed temperature of the membrane is varied and the effect of the same on the optimal efficiency is studied. Maximum membrane temperatures of 900°C, 1000°C and 1100°C are considered, and the procedure described above is used to perform the optimization in order to obtain an optimal efficiency. The results of this study are plotted in Figure 2-4. Appendix A shows detailed optimization results of zero and partial emissions cycles for membrane temperatures 900°C, 1000°C and 1100°C. It is observed that setting the maximum allowed membrane temperature to 900°C leads to the highest efficiency, whereas 1100°C corresponds to the lowest efficiency for a given CO_2 emission. Subsequent results (see also Figure 2-6), demonstrate that efficiency is monotonically increasing with temperature up to 850°C and monotonically decreasing for higher temperatures. Because the temperature of "COMBPROD" is fixed (1200°C), a greater value of the ITM membrane temperature (which is fixed by fixing "PERMEATE" stream temperature) indicates that the temperature of stream "GTIN" is lower, which implies a lower efficiency. Thermodynamically, a lower membrane temperature is seen to be beneficial. The reason for this is described in the next section. From Figure 2-5, it is inferred that although a lower value of the maximum allowed membrane temperature is thermodynamically beneficial, the total power produced by the power plant per unit surface area of membrane used is lower as explained in Section 2.3.4. Figure 2-5 shows the power produced per unit area of membrane used, for maximum membrane temperatures of 900°C, 1000°C and 1100°C. A trade-off is between thermodynamic superiority and economic inferiority is clearly noticeable. Simultaneous economic and thermodynamic optimization may provide a better idea of the effect of the maximum allowed membrane temperature.

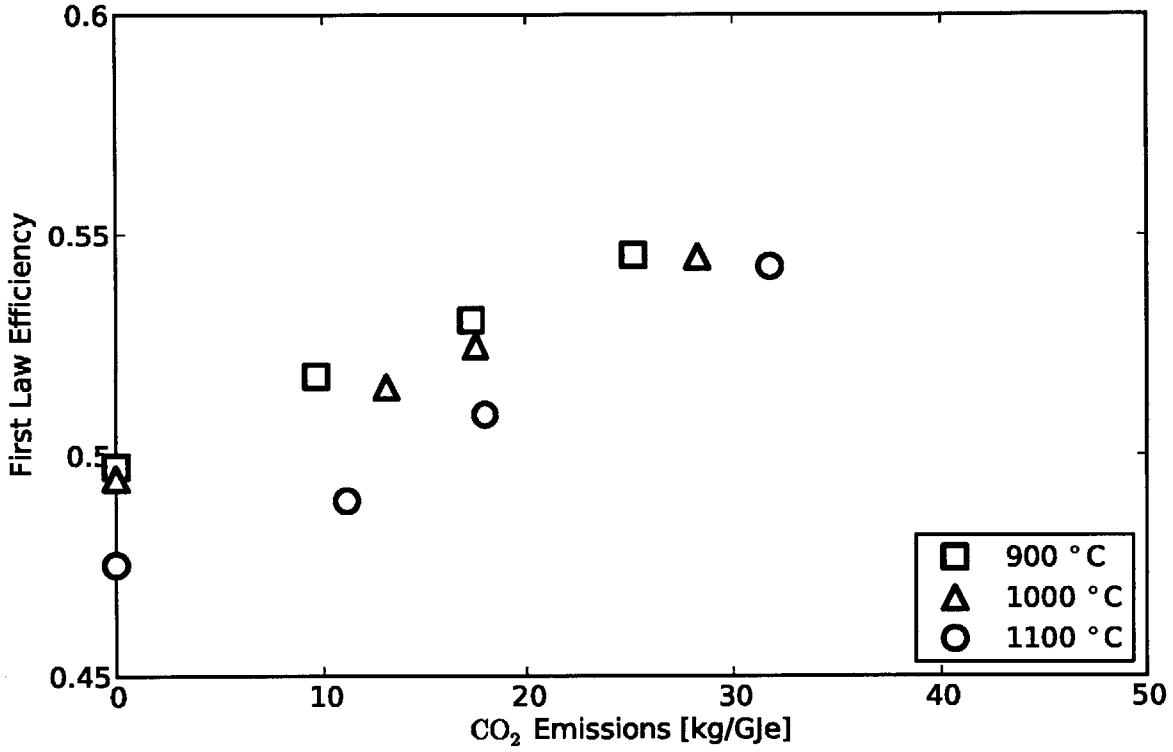

Figure 2-4: Variation of efficiency with maximum allowed membrane temperatures: 900°C, 1000°C, 1100°C for different CO_2 emissions keeping net volume and surface area of the membrane fixed.

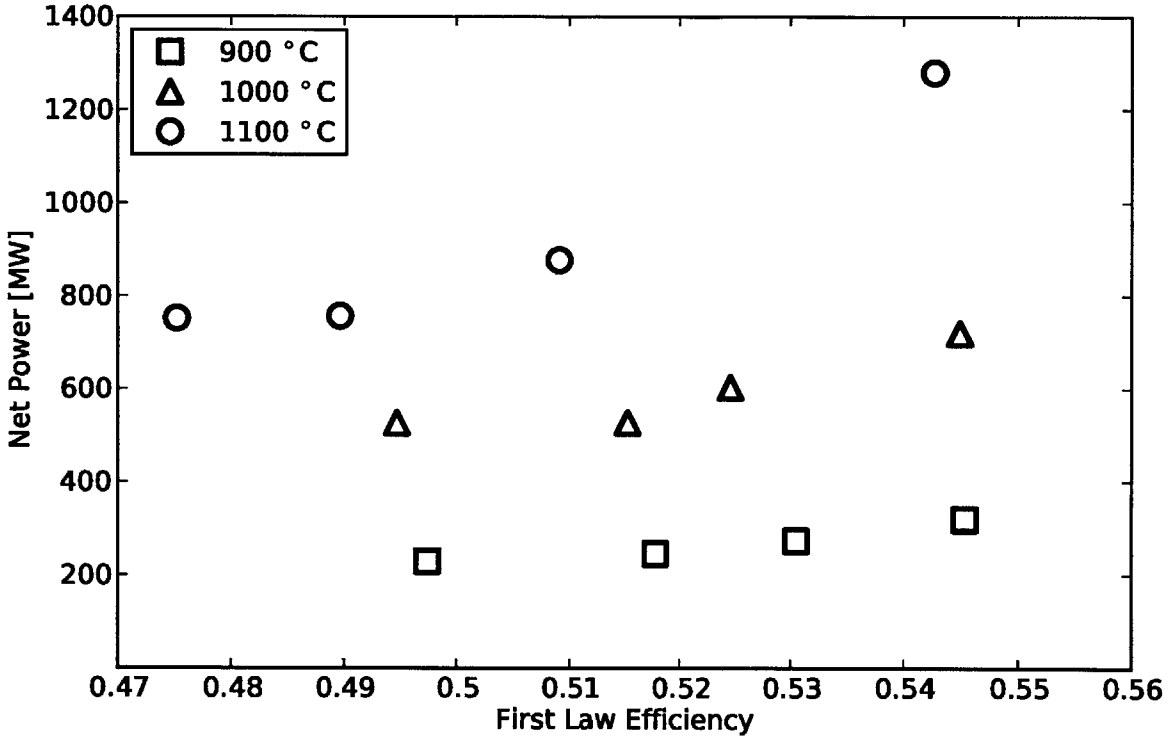

Figure 2-5: Net power produced for maximum allowed membrane temperatures: 900°C, 1000°C, 1100°C for different CO_2 emissions keeping net volume and surface area of the membrane fixed.

2.3.4 Effect of membrane temperature on efficiency and power output for fixed turbine inlet temperature

In this section, variations of efficiency and power output of a partial emissions power cycle with turbine inlet temperature set to its maximum allowed value of 1300°C are shown. This is obtained by adding sufficient fuel in the after-burner. As a consequence, CO_2 capture is not constant. Figure 2-6(a) shows the effect of membrane temperature on efficiency. As the membrane temperature decreases, efficiency increases till the membrane temperature reaches about 850°C, after which efficiency starts decreasing.

Figure 2-6(b) shows that as the membrane temperature decreases, power output decreases dramatically. This is because as the temperature decreases, O_2 separation is also reduced since the ITM area is held constant at 400 m^2. Consequently, fuel required decreases, since fuel required is determined by the stoichiometric amount needed to burn the separated O_2. This implies that the air flow rate into the system, which is used to maintain a fixed temperature of combustion products from the combustor, decreases. Thus, the power output is reduced. It is interesting to note that as the membrane temperature decreases from 1100°C to 780°C, air flow rate rapidly decreases from approximately 85 kmol/s to approximately 7 kmol/s. This rapid decrease of airflow rate results in a corresponding rapid reduction in power output.

The pinch of "LHEX-ITM-HHEX" heat exchanger network occurs at LHEX for higher membrane temperatures. The recycle ratio of flue gas from the combustor is determined to maintain the pinch of heat exchanger "LHEX" at 10°C. Figure 2-7(b) shows that the pinch of the heat exchanger "HHEX" decreases as membrane temperature is reduced till approximately 850°C, after which it is held at 10°C by varying the recycle ratio of the flue gas. The pinch of heat exchanger HHEX is equal to 70.7°C for membrane temperature equal to 1100°C, and decreases as the membrane temperature is reduced till about 850°C. Below 850°C, to avoid occurrence of cross-over in the heat exchanger "LHEX", preheater temperature is lowered while holding the pinch in the heat exchanger "HHEX" constant by varying the recycle ratio of flue gas. This results in an increase in the temperature of

stream "GTIN" (Figure 2-7(a)), which is further heated by the after-burner in the partial emissions cycle as the membrane temperature reduces, till it reaches 850°C. After this, the temperature of the stream "GTIN" remains constant as the pinch of heat exchanger "HHEX" is held constant. Higher temperature of stream "GTIN" means lower fuel ratio ($\frac{\text{Fuel to "AFTERBURNER"}}{\text{Fuel to "COMBUSTOR"}}$) required to attain the maximum allowed turbine inlet temperature equal to 1300°C. This implies higher efficiency as membrane temperature is reduced till approximately 850°C, after which efficiency decreases.

2.3.5 Effect of membrane temperature on efficiency and power output for fixed CO_2 emissions

For fixed turbine inlet temperature, as the membrane temperature is reduced, temperature of stream "GTIN" increases. Hence, the fuel ratio to maintain gas turbine inlet temperature reduces, and efficiency increases. For membrane temperature less than approximately 850°C, since the pinch of heat exchanger "HHEX" is fixed at 10°C, fuel ratio remains almost constant to maintain fixed gas turbine inlet temperature. On the same basis, for fixed CO_2 emissions and fuel ratio, efficiency increases with decrease in membrane temperature because the gas turbine inlet temperature increases as the membrane temperature is decreased till it reaches approximately 850°C, after which efficiency decreases.

2.4 Conclusions

Optimization of zero and partial emissions cycles results in a significant increase in efficiency. For maximum ITM temperature 1000°C, the efficiency of partial emissions cycles after optimization is greater than the efficiency of the corresponding combination of an AZEP100 and a combined cycle. However, the difference is not sufficiently large to make a definite conclusion about the feasibility of the partial emissions cycles. An analysis of the effect of the maximum allowed membrane temperature shows that AZEP cycles have a thermodynamic advantage for lower membrane temperature, i.e., efficiency increases as the membrane tem-

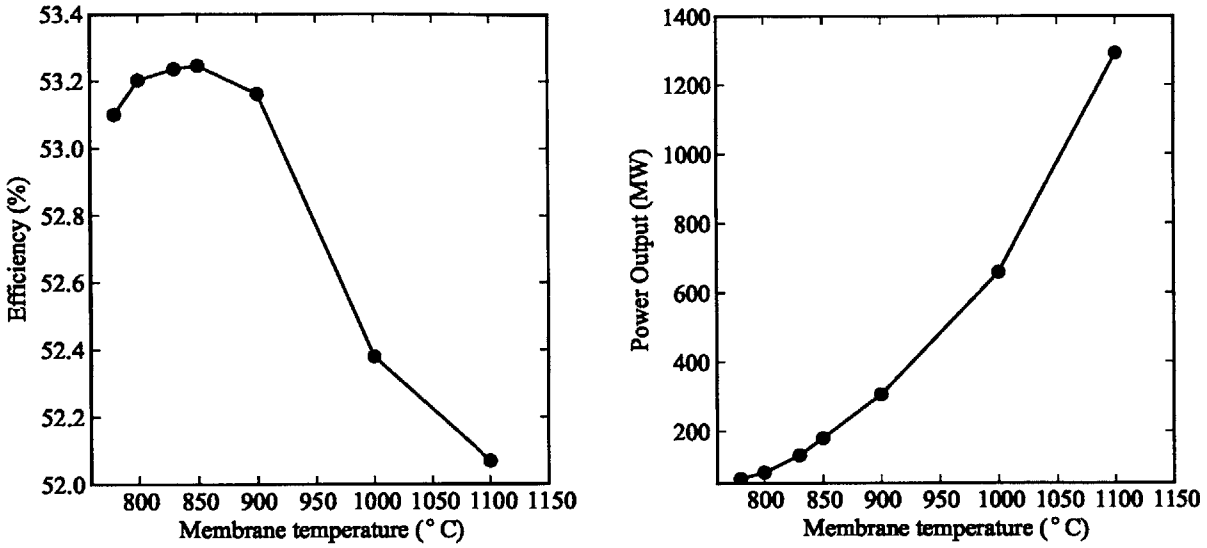

(a) (b)

Figure 2-6: Variation of (a) efficiency and (b) power output of a partial emissions AZEP cycle with maximum allowed membrane temperature (without optimization) with fixed ITM area and turbine inlet temperature.

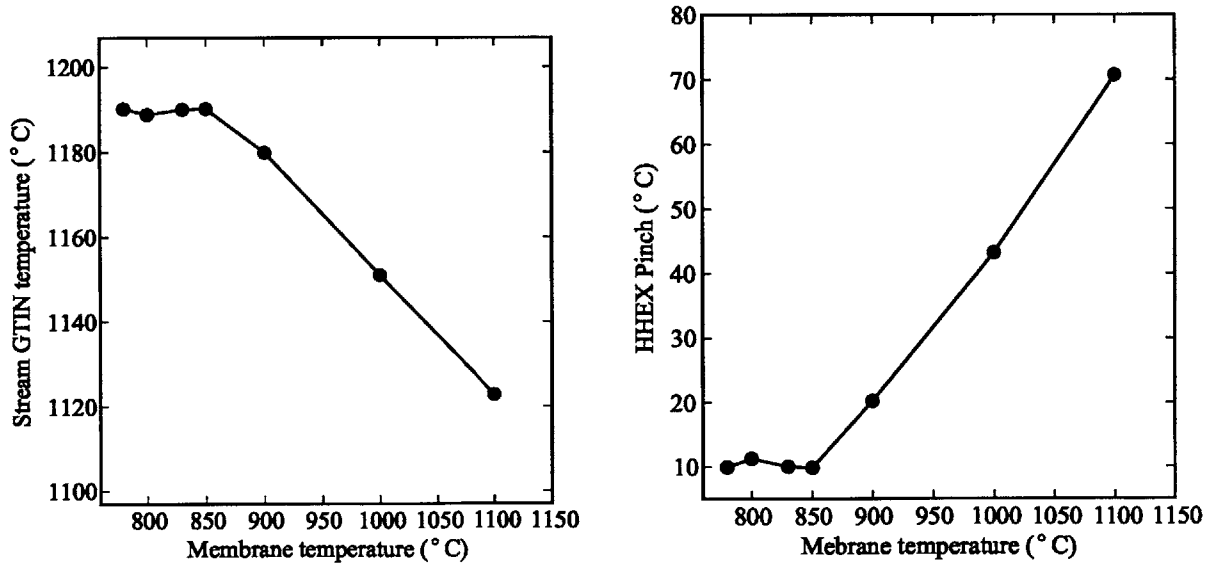

(a) (b)

Figure 2-7: Variation of (a) stream "GTIN temperature" and (b) pinch of heat exchanger HHEX of a partial emissions AZEP cycle versus maximum allowed membrane temperature (without optimization) with fixed ITM area and turbine inlet temperature.

perature is reduced till maximum membrane temperature reaches about 850°C, after which efficiency starts decreasing. At the same time, decreasing the ITM membrane temperature results in a dramatic decrease in power output for fixed ITM size. Therefore, simultaneous optimization of economic cost and thermodynamic efficiency may provide a better understanding of the trade-offs between the two.

Chapter 3

Solar-Thermal Hybridization of Advanced Zero Emissions Power Cycle

3.1 Introduction

Renewable sources of energy such as solar energy are gaining importance because of the worldwide large insolation, relatively low operating cost and CO_2 emissions. Concentrated solar thermal (CST) is one of the most widely used methods for utilizing solar energy for power production. CST technologies use collectors (e.g., mirrors) that optically concentrate the sun's rays on to a receiver, which operates at a relatively high temperature. A concentrated solar receiver is either directly used to heat the power plant working fluid as in direct steam generation (DSG) or to heat the heat transfer fluid (HTF) which is then used to heat the power plant working fluid [36]. Different types of concentrated solar receivers include parabolic troughs, Fresnel reflectors [45, 46], central receiver systems [47–50] and solar dish systems [46]. Parabolic trough is the most widely used form of CST technology [36]. Parabolic troughs use a single-axis tracking parabolic mirror to concentrate solar radiation on to a receiver pipe at the focal point, which contains the HTF or the power plant work-

ing fluid [36]. The receiver of the parabolic trough solar collector is called Heat Collector Element (HCE). The HCE consists of an absorber pipe through which the HTF flows. The absorber is typically made of stainless steel with a special selective coating on the outer surface to provide the required optical properties. A glass envelope protects the absorber pipe from material degradation and reduces heat losses. The operating temperatures of parabolic troughs can be as high as approximately 670 K. The highest reported instantaneous solar to electrical energy efficiency of parabolic troughs is about 20% [45, 46]. Solar to electrical energy efficiency is defined as

$$\eta_{\text{sol-elec}} = \frac{\dot{W}_{\text{solar}}}{\dot{Q}_{\text{solar}}} \tag{3.1}$$

where $\dot{W}_{\text{solar}}$ is the net power output of the solar only plant, and $\dot{Q}_{\text{solar}}$ is the solar energy rate input [51]. $\dot{Q}_{\text{solar}}$ is defined as $\dot{Q}_{\text{solar}} = \dot{q}_{\text{DNI}} \cdot A$, where $\dot{q}_{\text{DNI}}$ is the direct normal irradiance (DNI), and A is the projected normal reflective area of the collector. The projected normal reflective area has been used in the literature for calculating thermodynamic parameters such as efficiency [51]. But it should also be noted that the actual area of the mirror is approximately 1.5 times larger than the projected area [52, 53].

The major disadvantages in the use of solar energy are the requirement for large collector area, which leads to higher initial costs compared to conventional fossil fuel power plants [54], and the variability of supply throughout the day and year. This results in intermittent power production and requires some mode of energy storage in order to meet a given power demand profile. Hybrid concentrated solar-fossil fuel power generation may provide a solution to these problems [2, 36, 51, 55–58]. Also, hybrid power plants, in principle, can have thermodynamic synergies, which make them more attractive. Several hybrid power cycles have been proposed in the literature (e.g., see [36] and references therein).

Power plants with CCS can be considered promising candidates for solar-thermal hybridization because any increase in efficiency or decrease in the fuel requirement seems doubly rewarding [59, 60]. For fixed electrical power requirement, solar-thermal hybridized CCS power plants utilize solar energy to fulfill a part of the power plant energy requirement

rather than using fossil fuels. This reduces the amount of fossil fuel burned, which in turn lowers the amount of CO_2 emissions captured. The decrease in CO_2 emissions results in a lower energy requirement for separation and sequestration of CO_2, which further decreases the fuel input required. Hence, decreasing the fuel requirement by supplementing it with solar energy seems to be doubly rewarding. However, a disadvantage of using CCS power cycles for solar-thermal integration is that efficiency of CCS power plants are lower than the conventional combined cycles due to the penalties associated with the CCS. Solar-thermal hybridization with different types of CCS power plants, such as post-combustion capture, and oxy-combustion, have been proposed in the literature. Pak et al. [61, 62] proposed an oxy-combustion based solar-thermal hybrid power generation system (STHS). The STHS is constructed based on a gas turbine power generation system, where instead of air, the working fluid is steam produced by the solar subsystem. Based on a similar concept, Goau et al. [41] proposed an advanced oxy-fuel hybrid power system (AHPS). The difference between the two is that the former is a simple gas turbine cycle whereas the latter is an alternative recuperative cycle [63]. The authors found that AHPS is more efficient than STHS. However, both of these cycles utilize conventional air separation methods to produce air. On the other hand, the present work proposes and analyzes solar-thermal integration for an AZEP cycle, which uses membrane-based technology to separate air.

The concept explored herein is integrating the solar-thermal subsystem with an AZEP cycle [16, 20, 25–29] with 100% CO_2 capture. AZEP cycles are a class of oxy-combustion power plants, which use an ITM to separate oxygen from air. The penalties incurred during the separation when using an ITM are significantly lower compared to conventional cryogenic air separation methods, which have very low second-law efficiencies [7, 20]. Hence, AZEP cycles are one of the most promising CCS power plant options [64].

As seen in Section 3.2, all the solar-thermal integration schemes considered herein are with the bottoming cycle of the AZEP cycle. The temperature range of the working fluid of the bottoming cycle (water/steam) considered here is between 298-735 K, which predominantly overlaps with the range that can be achieved by using a parabolic trough. The temperature

ranges obtained using a central receiver system is 850-1070 K [46], and that obtained using solar dish technology is 870-1020 K [46–50]. Both of these ranges are above the maximum allowed steam turbine inlet temperature of 841 K due to material constraints [65]. Linear Fresnel reflectors are used when the maximum temperature of the HTF is required to be below 520 K [66]. Therefore, the temperature ranges that can be achieved by other CST technologies are not appropriate for integrating with the bottoming cycle of the AZEP cycle (Section 3.2). For the integration schemes considered here, a parabolic trough system is most suitable for solar-thermal hybridization.

The initial idea of solar-thermal integration of AZEP cycles was proposed by Mancini and Mitsos [59], albeit without any specifics or analysis. A preliminary analysis was performed by El-Khaja and Mitsos [60]. In this chapter, four different integration schemes are proposed including vaporization, preheating, heating of intermediate-pressure turbine inlet stream, and heating of low-pressure turbine inlet stream. The parabolic trough is modeled using Aspen Custom Modeler® and integrated with an AZEP cycle modeled in Aspen Plus® and JACOBIAN. An AZEP cycle [16, 20, 25–29] consists of a Brayton-like top cycle integrated with an ITM, a triple pressure HRSG bottoming cycle and CO_2 separation and purification unit. For the different integration schemes proposed herein, the profiles of power output versus time (in hours) for the duration of solar irradiance on summer and winter solstices, are compared with each other. It is found that vaporization integration scheme has the highest power output among all of them for both the summer and winter solstices. A hybrid power plant is considered viable if the power output from the hybrid power plant is greater than the sum of the power outputs from corresponding stand-alone AZEP cycle and solar-thermal power cycle. Based on this criterion, vaporization and heating of intermediate-pressure turbine inlet stream are found to be promising integration schemes. This criterion is equivalent to having incremental solar efficiency higher than the efficiency of the reference solar plant. In order to compare the present schemes with different hybrid technologies without CCS that have been proposed in the literature, the annual incremental solar efficiency metric is used.

3.2 Different Integration Schemes

This section explains the four schemes for solar-thermal integration with the bottoming cycle of AZEP cycle: vaporization of high-pressure water, preheating of high-pressure water, heating of intermediate-pressure turbine inlet stream, and heating of low-pressure turbine inlet stream. Vaporization and preheating are widely studied integration schemes for conventional combined cycles [2, 36, 57, 67]. These have been extended herein for solar hybridization of the AZEP cycle. The result obtained herein is that the vaporization scheme performs better than a preheating scheme. This is consistent with what has been reported in the literature for hybrid cycles without CCS [67]. Vaporization and preheating are considered only for high-pressure water. As heat needed to vaporize or preheat the high-pressure water stream is added at higher temperature compared to intermediate- or low-pressure water streams, the efficiency of the hybrid power cycle is higher. The intermediate-pressure turbine inlet stream temperature (600 K) is slightly higher than the boiling point of water at 100 bar (585 K). Therefore, heating of intermediate-pressure turbine inlet stream adds solar energy at a temperature range of 600 K - 660 K, which is higher than the temperature at which solar energy is added to the vaporization scheme (585 K), and the temperature range at which solar energy is added to the preheating scheme (340 K - 560 K). Since adding heat at higher temperature is beneficial, heating of turbine inlet streams is thought of as a good starting point. However, to determine the best solar-thermal integration scheme, structural optimization may be needed.

Therminol-VP-1 is used as the HTF for all the integration methods except preheating. For vaporization and heating of intermediate and low-pressure turbine inlet streams, solar energy concentrated by the parabolic trough is used to heat Therminol, which is in turn used to heat the working fluid in the bottoming cycle (water) in a heat exchanger. In the preheating scheme, the solar subsystem is directly used to heat high-pressure water after it is pressurized by the pump, and before it enters the flash drum.

Reference plant: The reference plant considered here is an AZEP cycle with 100% CO_2 capture. The AZEP cycle [16, 25–29] is one of the most promising options of oxy-combustion

CCS technology. As explained in Chapter 1, it is a combined cycle — the top cycle of the zero emissions or partial emissions cycles is a Brayton-like cycle with an ITM air separation unit and a combustor. The reference plant considered here is an AZEP cycle with 100% CO_2 capture with ITM area equal to 400 m^2.

Vaporization: As shown in Figure 3-2, in this scheme, the solar subsystem is used to vaporize the high-pressure water. The high-pressure saturated liquid from the flash drum "HPDRUM" is heated by the flue gas "PRODBOTM" in the heat exchanger "B16" to form a two-phase mixture. After this, the high-pressure stream (two-phase water) is further heated by Therminol-VP-1 in a heat exchanger "B1". Therminol-VP-1, the HTF, is heated by the parabolic trough system. The high-pressure stream is then allowed to vaporize till the heat exchanger "B1" reaches a pinch of 5 K. Depending on the DNI and the angle of incidence, the outlet stream from heat exchanger "B1" is either completely or partially vaporized. Also, in some cases, with high DNI values (e.g., noon of June 21), the concentrated solar energy is higher than the amount required to completely vaporize the high-pressure stream. In such cases, the intermediate-pressure stream was also passed through the heat exchanger "B1" and allowed to partially vaporize, to utilize the solar energy completely.

Preheating: As shown in Figure 3-3, in this scheme, the solar subsystem is used to preheat the high-pressure water after it exits the high pressure pump "HPPMP", and before it enters the high-pressure flash drum "HPDRUM". Even with highest DNI reported in the year 2008, the high-pressure stream heated by the parabolic trough does not reach the boiling temperature. Hence, solar energy concentrated using the parabolic trough is completely utilized to heat the high-pressure stream. Therefore, temperature outlet of the parabolic trough in this integration method varies with DNI. As seen in Figure 3-3, high-pressure stream, after being compressed by the pump "LPPMP" is preheated directly by the solar trough system before it enters the high-pressure flash separator "HPDRUM" and then enters the heat exchanger "HPEV" and "HPSP".

Heating of intermediate and low-pressure turbine inlet streams: In this scheme, the solar subsystem is used to heat the intermediate-pressure turbine ("IPST") inlet stream

or the low-pressure turbine ("LPST") inlet stream. As shown in Figure 3-4, the intermediate-pressure turbine inlet stream "IPSTIN" is heated in the heat exchanger "B1" with the HTF, and the outlet stream "IPSTHEAT" from the heat exchanger "B1" is then expanded through the intermediate-pressure turbine "IPST". In the case of heating of the low-pressure turbine ("LPST") inlet stream, the stream "LPSTIN" is heated in the heat exchanger "B1" instead of "IPSTIN" and the heated stream is similarly expanded through the low-pressure turbine "LPST". Figure 3-4 shows 4 turbines at different pressure levels. The high-pressure turbine "HPST" has an inlet pressure of 100 bar and exit pressure of 25 bar. The turbine inlet temperature of "HPST" is approximately 733 K, which is greater than the maximum operating temperature of parabolic troughs reported in the literature (670 K). Hence, the parabolic trough cannot be used to heat the inlet stream to the high-pressure turbine. In this work, heating of inlet stream to the intermediate-pressure turbine "IPST" at 25 bar and low-pressure turbine "LPST" at 5 bar are considered. For fixed fuel input, heat addition at higher temperature yields a higher efficiency compared to heat addition at lower temperature. Hence, heating of inlet stream to turbine "LASTST" (Figure 3-4), which is at a lower temperature compared to the other three turbines, is not considered.

3.3 Modeling

3.3.1 Parabolic Trough Model

The HCE of the parabolic trough is modeled in Aspen Custom Modeler®. The model uses a one-dimensional pseudo steady-state energy balance about the collector and the HCE. The model, assumptions and the parameter values used are based on the NREL technical report [4]. A brief description of the model is given in Appendix B. The energy balance accounts for DNI incident on the collector, and optical losses and thermal losses from the HCE. The model takes as input the inlet temperature, pressure and fluid properties, and determines the heat transfer rate and the outlet temperature of the HTF. The space between the glass envelope and the absorber pipe (annulus) is assumed to be filled with air at low-

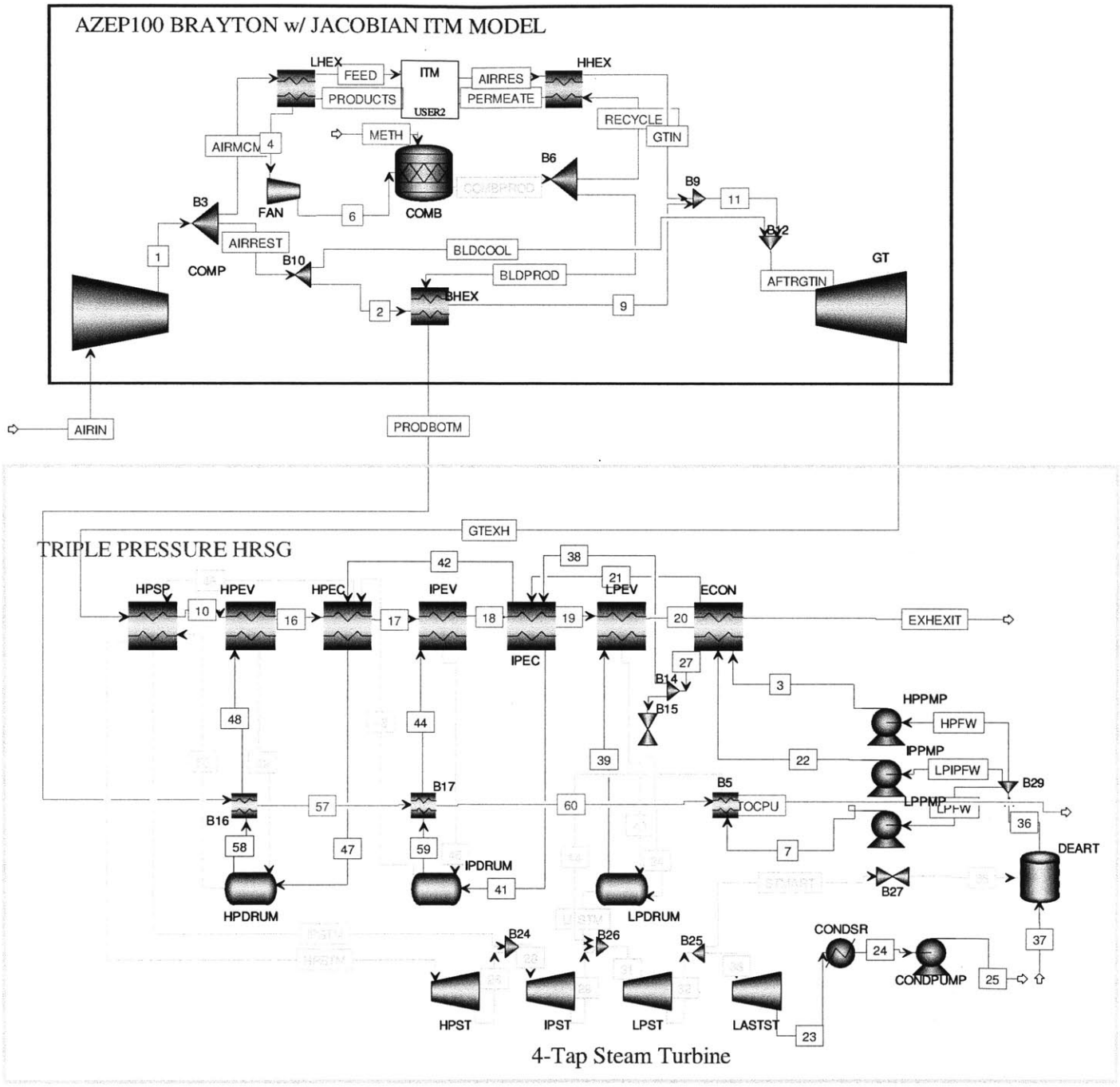

Figure 3-1: AZEP100 cycle process flow diagram. Bottoming cycle is a triple pressure HRSG.

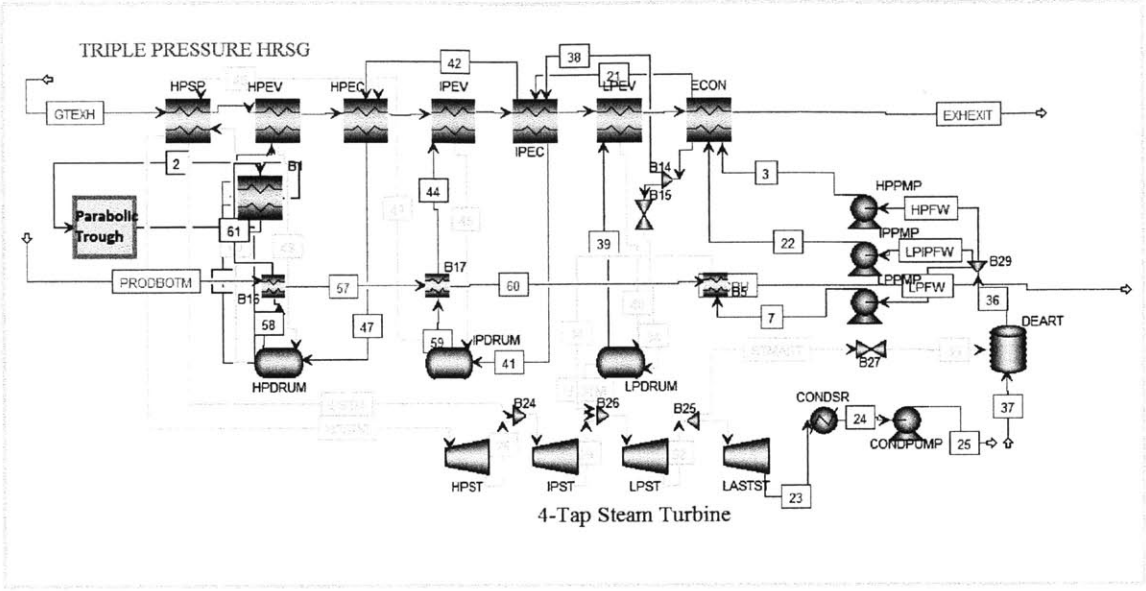

Figure 3-2: Solar subsystem integrated with the bottoming cycle to vaporize high-pressure stream in the bottoming cycle.

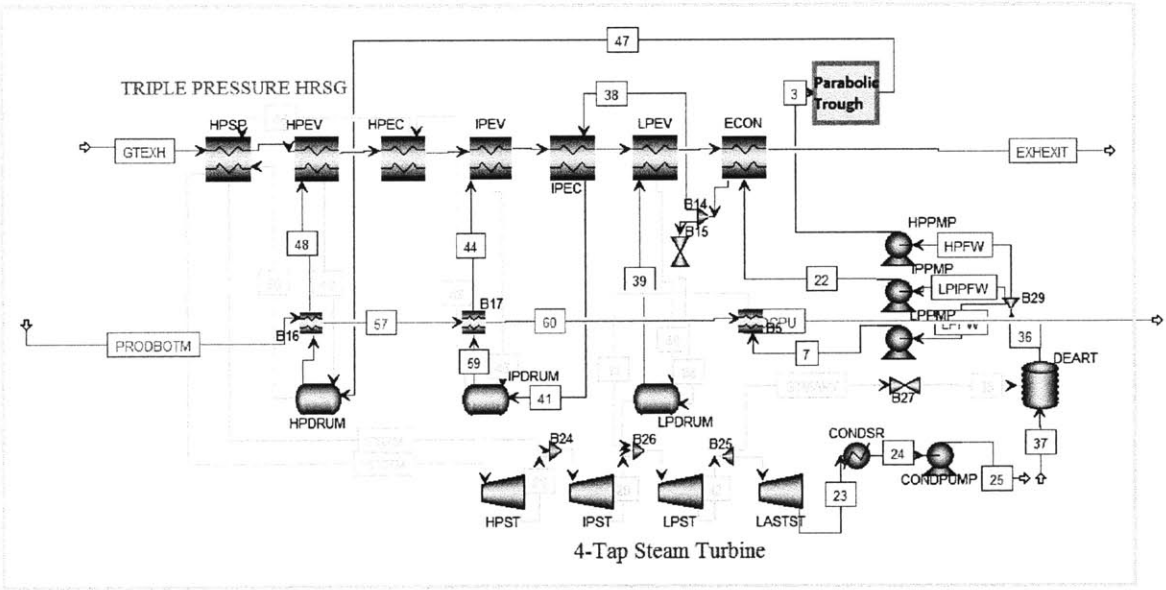

Figure 3-3: Solar subsystem integrated with the bottoming cycle to preheat high-pressure stream in the bottoming cycle.

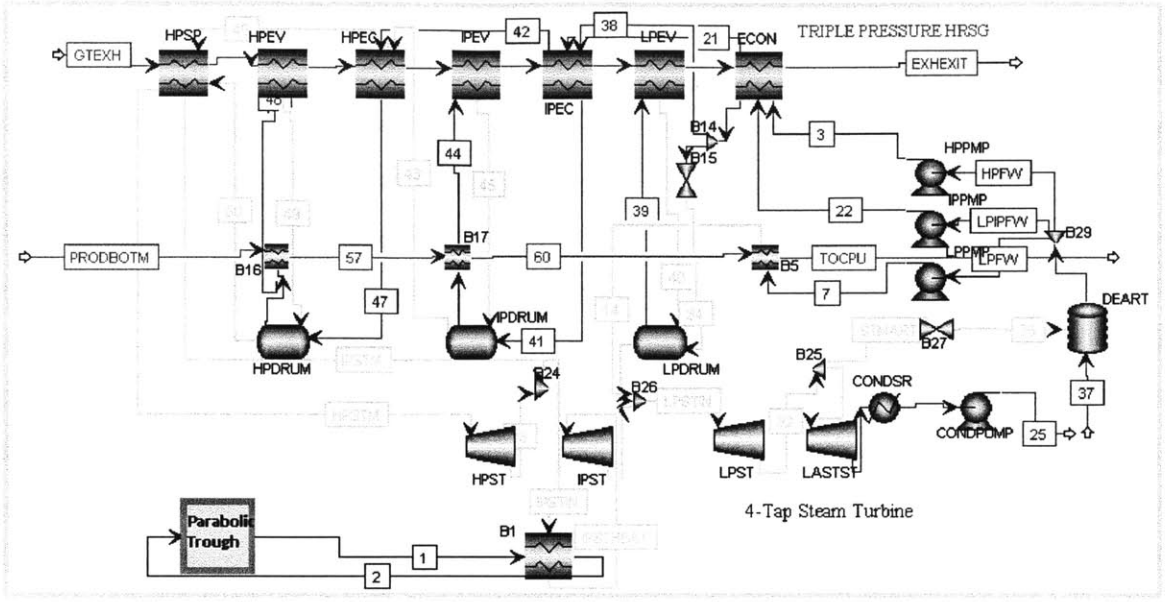

Figure 3-4: Solar subsystem integrated with the bottoming cycle to heat the intermediate-pressure turbine inlet stream in the bottoming cycle.

pressure.

3.3.2 Advanced Zero Emissions Power Cycle

The AZEP cycle with 100% CO_2 described in Chapter 1 is used here. Herein, methane is used as the fuel and the ITM area is fixed at 400 m^2. A standard triple pressure HRSG cycle with pressure levels at 100, 25 and 5 bars is used as the bottoming cycle for the AZEP100 cycle.

3.3.3 Model Design Specifications

Model specification of parabolic trough

The solar share based on energy input, a commonly used metric to characterize hybrid cycles, is defined as [68]

$$X_{s,i} = \frac{\dot{Q}_{solar}}{\dot{Q}_{fuel} + \dot{Q}_{solar}} \tag{3.2}$$

and describes the fraction of solar energy input to the total energy input of a hybrid power cycle.

The heating rate of the fuel (methane) is defined as $\dot{Q}_{fuel} = \dot{n}_{fuel} \cdot \text{LHV}$, where LHV is the lower heating value (per mole) of the fuel, and $\dot{n}_{fuel}$ is the molar flow rate of the fuel.

The total projected area of the parabolic trough is calculated such that the maximum solar share based on energy input is 0.3. Typical values of solar share considered in literature are between 20-50% [1, 49]. The typical value of annual solar share is about 30% [1]. Moreover, typical large solar power plants have a power output of about 100 MW [69], which is of the same order of magnitude as the electricity produced due to addition of solar subsystem to the AZEP cycle.

For the sake of simplicity, $\dot{n}_{fuel}$ is assumed constant in the present simulations. A constant fuel flow rate results in easy operation of the top cycle. But the power produced varies with the variation in DNI and angle of incidence. Thus, with the assumption of a constant fuel flow rate, the electricity production cannot be controlled, and therefore need not necessarily match the electricity demand. Hence, although hybridization can eliminate the need for storage in principle, this advantage is not leveraged here.

The DNI data used herein is obtained from the weather station at King Fahd University of Petroleum and Minerals (KFUPM) in Dhahran, Saudi Arabia. The measurements are from the year 2008 and are available on an hourly interval for the entire year. DNI values lower than 150 W/m^2 are not considered since these do not provide additional power to the AZEP reference plant. Figure 3-5 (a) and (b) show the variation of DNI and angle of incidence between the normal to the parabolic trough and solar rays for March 21, June 21 and December 21, 2008. It can be seen from Figure 3-5 (a) that DNI data are not perfectly symmetrical around noon for each day. For example, it is seen that on March 21, 2008, the DNI is not maximum at noon.

The maximum solar share based on energy input has been assumed to be 0.3 as mentioned

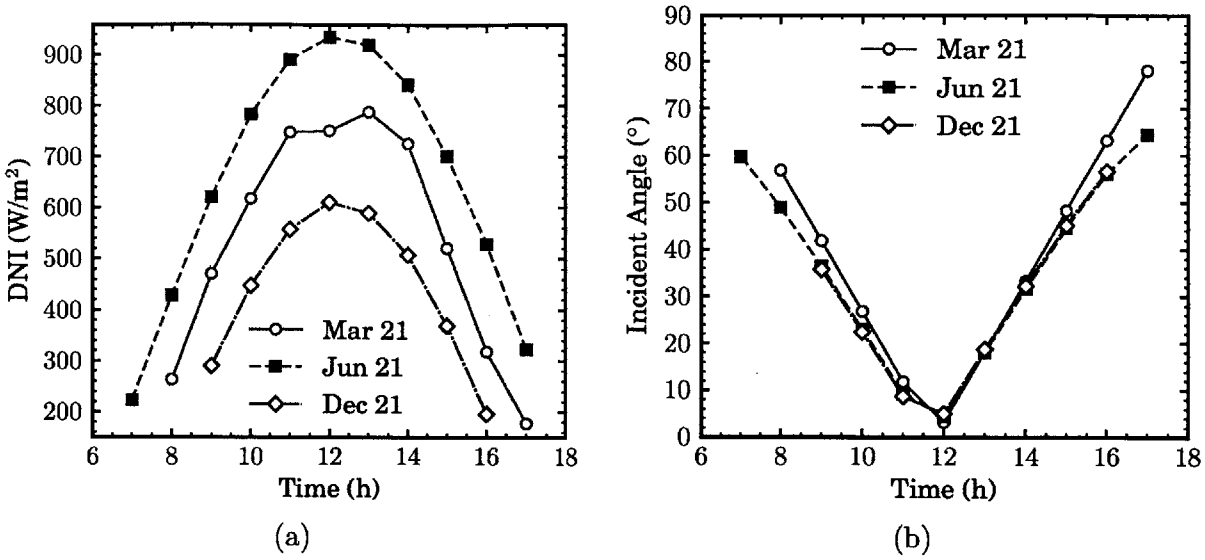

Figure 3-5: Variation of (a) DNI, and (b) angle of incidence between the solar rays and collector aperture for 3 days of the year 2008 (March 21, June 21, December 21).

Parameter	Value
Solar share based on energy input	0.3
Total trough area	3.9×10^5 m^2
Number of parabolic troughs in parallel	150
Area of each parabolic trough	2.6×10^3 m^2
Aperture width	5.76 m
Length of receiver pipe of each parabolic trough	450 m

Table 3.1: Fixed design parameters of the trough model.

previously, which together with a maximum irradiance of 1000 W/m^2 obtained at KFUPM weather station for the year 2008, and fuel flow rate of 1.1 kmol/s, leads to a parabolic trough area of $A = 3.9 \times 10^5$ m^2.

The values of various fixed design parameters used in modeling of the parabolic trough are listed in Table 3.1. Appendix B gives a detailed description of the procedure used to obtain these values.

The trough is assumed to be oriented in the North-South direction [70]. To incorporate single-axis tracking into the model, the tilt of the parabolic trough is varied to obtain minimum angle of incidence between the normal to the parabolic trough and the solar rays. The

angle of incidence is calculated on an hourly interval as shown in Appendix C.

Model Specifications of AZEP cycle

Herein, the simulations are run for various DNI values obtained from the KFUPM weather station. This is in contrast to most solar-thermal hybridization simulations in the literature, which consider only one fixed value of DNI, often solar solstice at noon. Since the DNI data is available on an hourly interval, the simulations are performed on an hourly basis. A quasi steady-state assumption is used to model the AZEP cycle. The flow rate of water (working fluid) and the turbine inlet temperature in the bottoming cycle varies for different times of the day depending on DNI and angle of incidence. The turbine inlet and outlet pressures remain the same. Therefore, the flow rate and enthalpy change across the steam turbines vary throughout the day. This implies that the steam turbines do not always operate at their design point, leading to varying isentropic efficiency. The flow rate dependence of isentropic efficiencies of the turbines/compressors depends on the manufacturer. Therefore, for the sake of simplicity and to reduce the computational time, the isentropic and mechanical efficiencies of the turbines and compressors used herein are held constant. The isentropic and mechanical efficiencies of the steam turbines are fixed at 0.9 and 0.95 respectively, the isentropic and mechanical efficiencies of the gas turbines are fixed at 0.92 and 0.99 respectively, and the isentropic and mechanical efficiencies of the air compressor are fixed at 0.85 and 0.95 respectively. Since we assume constant isentropic efficiencies, the power output obtained could be an over-prediction. It should be noted, however, that high values of isentropic efficiencies can be obtained by varying the operational variables, and so the over-prediction is acceptable. Moreover, since optimization studies have not been performed, the actual estimate of work done is conservative.

Heat exchanger block "HeatX" in Aspen Plus® is used to model the HRSG®. This block uses a log mean temperature difference (LMTD) model to calculate the heat transfer rate. It uses a constant LMTD correction factor equal to 1, and the heat transfer coefficient is calculated for each zone of the exchanger. The areas of heat exchangers in HRSG are assumed

Integration Schemes	Value
Reference plant	1.4×10^5 m^2
Vaporization of high-pressure stream	1.1×10^4 m^2
Preheating of high-pressure stream	7.6×10^3 m^2
Heating of intermediate-pressure turbine inlet stream	1.4×10^5 m^2
Heating of low-pressure turbine inlet stream	1.4×10^5 m^2

Table 3.2: HRSG area for different integration schemes.

to be constant for each integration scheme. The following procedure is used to obtain the HRSG area for each integration scheme. First, the flow rate of water in the bottoming cycle is varied such that the pinch of HRSG is constant at 6 K for different DNI values. This is implemented in the form of a design specification in Aspen Plus®. Correspondingly, the HRSG area changes for each of the DNI values. The maximum such HRSG area obtained is then fixed as the HRSG area for the corresponding integration scheme. The simulations are then re-run for each integration scheme with fixed HRSG area. The HRSG area for different integration schemes are shown in Table 3.2, and are substantially different from each other.

The HRSG area for the vaporization integration scheme is lower than that of the reference plant because the area of "HPEV" (high-pressure evaporator) is reduced. Moreover, temperature difference between the hot and cold streams of the heat exchangers "IPEV", "IPEC", "LPEV", "ECON" are also greater because "HPEV" uses lesser thermal energy of the hot stream, leading to lower HRSG area. The area required for preheating integration scheme is the least among all because high-pressure stream no longer passes through heat exchangers "ECON", "IPEC", "HPEC" (Figure 3-3). The HRSG area for both heating integration schemes is the same as the reference plant, since this type of integration does not affect the HRSG.

3.4 Results and Discussion

Figure 3-6 shows the parabolic trough outlet temperature for three different days in the year 2008 – March 21, June 21, December 21. The summer and winter solstices are chosen

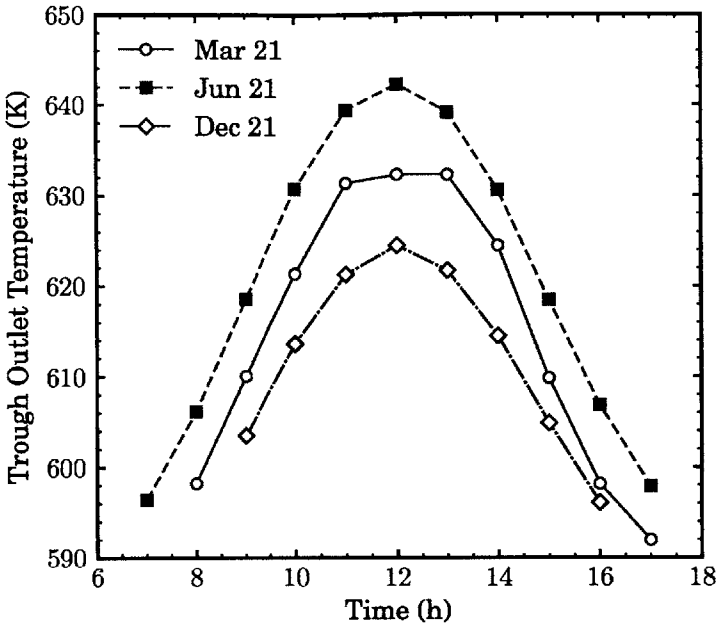

Figure 3-6: Outlet temperature of Therminol-VP-1 from the parabolic trough for 3 days of the year 2008 (March 21, June 21, December 21).

to represent days with high and low solar irradiance respectively, and the spring equinox, represents a day with intermediate solar irradiance. The input solar irradiance and the incident angle changes throughout the day, with the area of the trough fixed at 3.9×10^5 m^2 (as explained in Section 3.3.3). Figure 3-6 shows that maximum parabolic trough outlet temperature occurs at noon even when the DNI is not maximum at noon (March 21), which is explained by a low angle of incidence at noon.

The AZEP base cycle without solar-thermal hybridization represents a reference plant as previously explained in Section 3.2. For a given DNI, angle of incidence and fuel input, if the power output from the solar-thermal hybridized power plant is greater than the sum of the power outputs from stand-alone AZEP cycle and solar-thermal cycle, then the solar-thermal hybridized power plant is considered viable. If not, it is better to use the AZEP cycle and the solar-thermal cycle separately. This criterion is equivalent to having incremental solar efficiency higher than the efficiency of the stand-alone solar-thermal cycle. The power output $\dot{W}_{\text{AZEP+solar,ref}}$ of the reference combination of AZEP + Solar plants is calculated as

$$\dot{W}_{\text{AZEP+solar,ref}} = \dot{W}_{\text{ref}} + \dot{Q}_{\text{trough}} \cdot \eta_{\text{trough-elec,ref}} \tag{3.3}$$

where

$$\eta_{\text{trough-elec,ref}} = \frac{\eta_{\text{sol-elec,ref}} \cdot \dot{q}_{\text{DNI,nominal}} \cdot A}{\dot{Q}_{\text{trough,nominal}}} \tag{3.4}$$

where $\dot{W}_{\text{ref}}$ is the power output of the AZEP only reference plant, $\dot{Q}_{\text{trough}}$ is the heat transfer rate from the receiver pipe to the working fluid, $\dot{Q}_{\text{trough,nominal}}$ refers to the maximum heat added by the parabolic trough to the HTF, and $\dot{q}_{\text{DNI,nominal}}$ is the nominal (taken at maximal) DNI. $\eta_{\text{sol-elec,ref}}$ is the solar to electrical energy efficiency of the solar-thermal reference plant, and is taken as 0.2 (highest reported solar to electrical energy efficiency for a parabolic trough power plant) [45, 46]. It should be noted that $\eta_{\text{sol-elec,ref}}$ normally changes with time as the DNI changes. Its value of 0.2 used here is the maximum solar to electrical energy efficiency reported in the literature. Hence, a constant value of 0.2 is an over-estimate, and imposes tighter constraints on determining the viability of hybrid power plants. Figure 3-7 and Figure 3-8 compare the power output from the different integration schemes on June 21 and December 21 respectively. The integrated power cycle using the vaporization scheme is more efficient than the AZEP + Solar reference plant by 1.5% and 1.2% (corresponding to 0.65 and 0.52 percentage points) based on the efficiency computed by integrating the net power output throughout the day on June 21 and December 21 respectively (Figure 3-7 and Figure 3-8). Though the difference in power output between the vaporization scheme and AZEP + Solar reference plant is not high, it should be noted that the power output from the AZEP + Solar reference plants is an optimistic estimate, and optimization of the vaporization scheme would further increase its power output. Hence, vaporization of high-pressure stream can be considered to be a very promising hybridization scheme. Among the proposed integration schemes, the vaporization scheme of integration results in maximum power output, followed by heating of intermediate-pressure turbine inlet stream. Heating of low-pressure turbine inlet stream results in a lower power output

than heating of intermediate-pressure turbine inlet stream. Preheating hybridization scheme results in the lowest power output. Since this pattern holds for both the solstices, it is reasonable to expect that the same pattern would be observed throughout the year. The power output of the AZEP + Solar reference plant is between the power outputs resulting from the two heating integration schemes on June 21. On December 21, the power output of the AZEP + Solar reference plant is nearly the same as the power output obtained by heating of intermediate-pressure turbine inlet stream. The power output from heating of intermediate-pressure turbine inlet stream is also found to be greater than or equal to the AZEP + Solar reference plant, which is an optimistic estimate, as explained earlier. Therefore, vaporization and heating of intermediate-pressure turbine inlet stream can be viewed as promising integration schemes, and need to be further investigated.

In the vaporization hybridization scheme, the flue gas leaves the heat exchanger "HPEV" at higher temperature compared to the reference plant because a part of the high-pressure stream vaporization is done using the solar subsystem. This implies that in all of the heat exchangers that follow, the hot stream is at a higher temperature compared to the one in the reference plant. This higher temperature causes the total water flow rate into the bottoming cycle to increase in order to have a constant pinch of 5 K in HRSG. The water flow rate does not change in the heating of intermediate and low-pressure turbine inlet streams integration schemes, since the solar subsystem is just used to heat the inlet stream to the turbine and does not affect the temperatures in the HRSG. The increase in the water flow rate is significant and leads to a high power output in the vaporization scheme.

Heating the inlet stream of the intermediate-pressure turbine implies adding heat at higher temperature compared to heating the inlet stream of the low-pressure turbine. Since adding heat at higher temperature increases efficiency (compared to the same amount of heat added at a lower temperature), heating of intermediate-pressure turbine inlet stream results in a higher power output than heating of low-pressure turbine inlet stream.

Further, the power output from the preheating hybridization scheme falls below the reference plant power output when the solar irradiance is low, leading to negative incremental

solar efficiency. Note that negative incremental solar efficiency has been identified in the literature as a possibility [36]. Stream "47" (output from the parabolic trough in the pre-heating hybridized cycle) is not heated sufficiently when solar irradiance is low. This leads to a sub-cooled stream entering the flash drum as opposed to saturated stream entering the flash drum in the reference case. In turn, this lowers saturated vapor flow rate out of the high-pressure flash drum "HPSRUM" in the preheating hybridization scheme when compared to reference plant. The result is a lower flow rate to the high-pressure turbine "HPST", which leads to a low power output. However, it should be noted that the HRSG area required for this integration scheme is the least (see Section 3.2).

Different metrics [36] can be used to compare the solar-thermal hybridized AZEP cycle using the vaporization hybridization scheme with existing hybrid technologies in the literature. In this work, the incremental solar efficiency is used for comparison because it allows for comparison of both how efficiently solar energy is used, as well as the relative potential of various integration schemes. Evaluation of incremental solar efficiency on an annual basis enables comparison on a more comprehensive basis as the DNI and the angle of incidence varies throughout the year. In order to reduce computation time, 20 days equally spaced throughout the year are used as a representative sample to calculate the annual incremental solar efficiency. When 10 equally spaced days are used as a representative sample for the entire year, the value of incremental solar efficiency differs from that corresponding to a discretization with 20 equally spaced days by about 0.2 percentage points. This suggests that the discretization results in a substantial but acceptably large error. The power output from the best hybridization scheme, namely vaporization, throughout the day is shown in Figure 3-9 for various days of the year. The annual incremental solar efficiency is defined as

$$\eta_{\text{inc-sol-annual}} = \frac{W_{\text{hybrid,annual}} - \eta_{\text{ref}} Q_{\text{fuel,annual}}}{A \cdot \int_{\text{ann}} \dot{q}_{\text{DNI}} \, \mathrm{d}t} \tag{3.5}$$

where $W_{\text{hybrid,annual}}$ and $Q_{\text{fuel,annual}}$ are the total work output and fuel input respectively of the hybrid plant for the entire year, and η_{ref} is the efficiency of the AZEP only reference plant.

Figure 3-10 compares the proposed vaporization hybridization scheme with other hybrid technologies without CCS [1–3]. These references have been chosen for comparison because they report the annual incremental solar efficiency of the respective hybrid power plant. All the cycles from the literature reported here use a solar tower to concentrate the solar energy with the exception of combined cycle gas turbine (CCGT) systems, which use a parabolic trough. Solar reforming, Seville H1, Daggett H1, Seville M50, Daggett M50, CCGT Almeria, and CCGT LasVegas report solar share based on energy input values of 9.58%, 38.65%, 47.7%, 18.9%, 21.54%, 3% and 4.56% respectively. As seen from Figure 3-10, the annual incremental solar efficiency is substantially greater than all the existing hybrid technologies with the exception of CCGT LasVegas [2] and solar reforming cycle [3], which have higher incremental solar efficiency. Though CCGT LasVegas and solar reforming cycle have higher incremental solar efficiency, their input solar share is small. Figure 3-11 shows a graph of input solar share used and the incremental solar efficiency for different hybrid cycles in the literature and the proposed vaporization scheme. It suggests that there is a trade-off between the input solar share and incremental solar efficiency, i.e., plants with high solar share have low incremental solar efficiency. Figure 3-11 shows that CCGT LasVegas, solar reforming, Seville H1, Daggett H1 and the proposed solar hybridized AZEP cycle are more competitive than CCGT Almeria, Seville M50 and Daggett M50. The proposed solar hybridized AZEP cycle is seen to be equally competitive with the CCGT LasVegas, solar reforming, Seville H1, and Daggett H1 hybrid cycles in the sense of Pareto optimality. However, it should also be noted that the hybrid cycle under consideration is a solar-thermal hybridization of a fossil fuel plant with CCS, whereas others are not CCS technologies. CCS imposes additional constraints on the power plant. For example, CCGT power plants considered here have a higher steam turbine inlet temperature of 818 K, compared to hybrid AZEP cycles with a steam turbine inlet temperature of 733 K. This is achieved in CCGT plants by further heating the outlet stream from the parabolic trough with the flue gas from the gas turbine in the top cycle. This is not possible in hybrid AZEP cycles because the temperature of stream "GTEX", which is the outlet stream from the gas turbine, is low (approximately

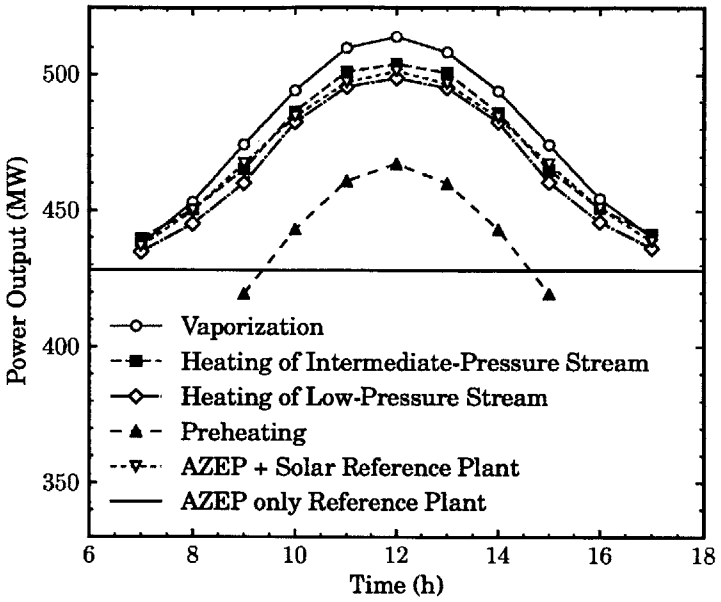

Figure 3-7: Comparison of different integration schemes for June 21 2008.

760 K). This is due to the fact that the maximum temperature that can be achieved in the top cycle is only 1473 K, which is limited by the combustor outlet temperature (Section 3.3.2), compared to higher temperatures (approximately 1573 K) that can be achieved in a conventional power plant. The solar reforming cycle [3] is an optimized hybrid cycle, whereas the hybrid AZEP cycle proposed herein is not optimized. Also the solar reforming cycle uses a solar tower CST technology, which has higher solar to electrical energy efficiency compared to a parabolic trough. It should be noted that none of the hybrid cycles listed here, except the solar reforming cycle, are optimized. Optimization studies could change the relative magnitudes of power output from the cycles shown. The solar hybridized AZEP cycle has a incremental solar efficiency comparable to plants in the literature without CCS, and this suggests that AZEP cycles are a promising option to be considered for solar-thermal hybridization.

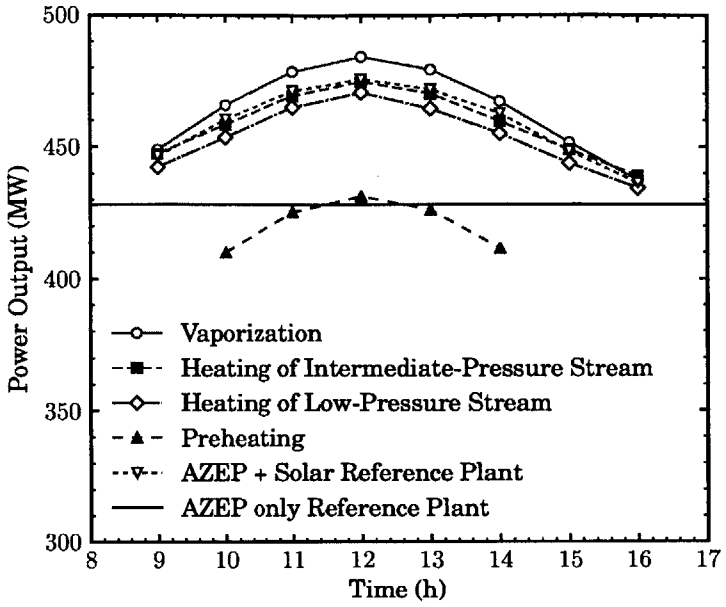

Figure 3-8: Comparison of different integration schemes for December 21 2008.

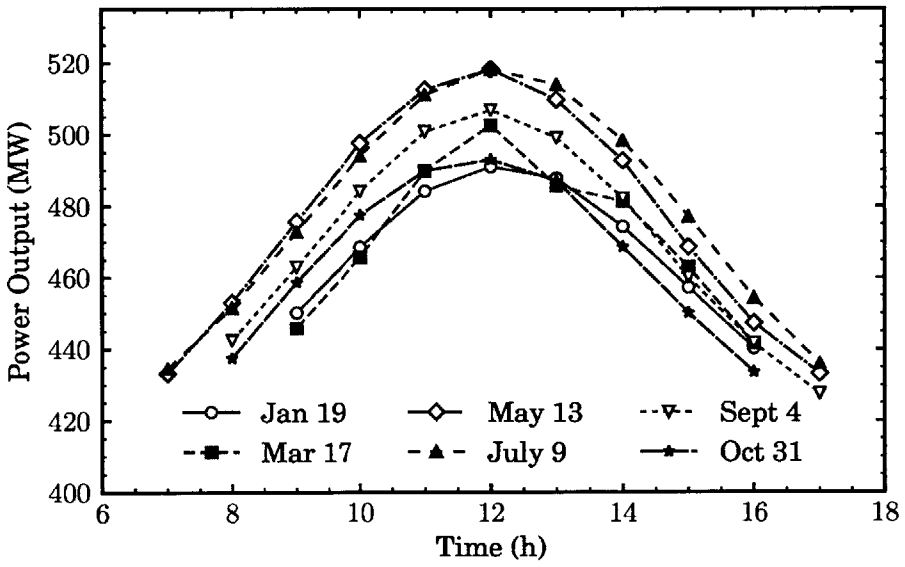

Figure 3-9: Power Output from vaporization hybridization scheme through out the day for various days in the year.

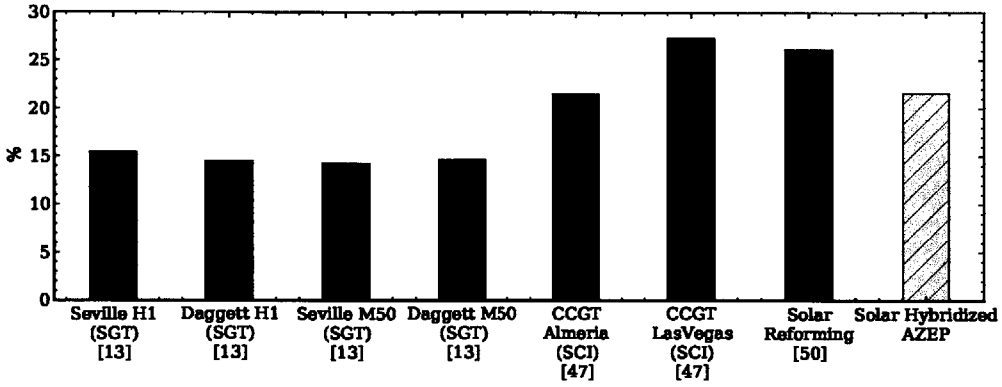

Figure 3-10: Comparison of annual incremental solar efficiency: SGT - Solarized Gas Turbine and SCI - Steam Cycle Integration [1–3].

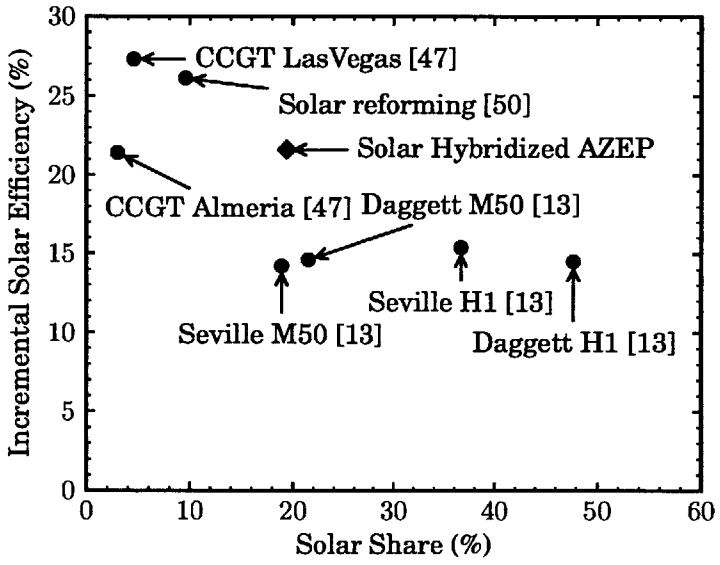

Figure 3-11: Trade-off between the incremental solar efficiency and solar share [1–3].

3.5 Conclusions and Future Work

Solar-thermal hybridization with an AZEP cycle is studied. Different integration schemes of the solar subsystems with the AZEP cycle including vaporization of high-pressure stream, preheating of high-pressure stream, heating of intermediate-pressure turbine inlet stream and heating of low-pressure turbine inlet stream are investigated. The vaporization scheme of integration results in maximum power output followed by heating of intermediate-pressure turbine inlet stream. This is followed by heating of low-pressure turbine inlet stream. Preheating has the lowest power output among the four integration schemes considered. Vaporization and heating of intermediate-pressure turbine inlet stream have power output greater than or equal to the sum of the power outputs from stand-alone AZEP cycle and solar-thermal cycle. Hence, they are promising integration schemes and need to be further investigated. Heating of intermediate-pressure turbine inlet stream and preheating are shown to be not viable. A comparison of annual incremental solar efficiency with existing hybrid plants without CCS shows that solar-thermal hybridization of an AZEP cycle with vaporization integration scheme proves to be better than most other hybridization schemes in the literature. Hybrid technologies with higher incremental solar efficiency have lower solar share. A comparison of technologies suggests a trade-off between input solar share and incremental solar efficiency. In the sense of Pareto optimality, the vaporization hybridization scheme is equally competitive with other hybrid technologies without CCS in the literature. It should also be noted that CCS imposes additional constraints on AZEP cycles which may lead to lower efficiency. Hence, AZEP cycles are one of the most promising options for solar-thermal hybridization. Moreover, optimization of this system can further increase the power output.

DSG with parabolic trough could also be a promising integration option to be used for vaporization scheme with AZEP cycle. DSG, a relatively new technology [71], eliminates the need for a heat exchanger to transfer heat from the HTF to the working fluid of the bottoming cycle, which results in lower irreversibilites and consequently, a higher efficiency. Optimization of the proposed integration schemes would help to accurately judge the viability of solar hybrid AZEP cycles. In this work, only the AZEP100 power cycle has been

considered. Integration with partial emissions AZEP cycles would also be interesting to explore, as these have higher efficiencies. Another advantage of partial emissions cycles is that they have higher turbine inlet temperature, which may allow them to overcome certain constraints imposed by CCS.

Appendix A

Optimization Results for AZEP Cycles with Different Membrane Temperatures

A.1 Membrane Temperature = 1000°C, CO_2 Capture = 87.7%, Fuel Ratio = $\frac{\text{Fuel to "AFTERBURNER"}}{\text{Fuel to "COMBUSTOR"}} = 14$

Table A.1: Results of Optimization of Top cycle (Membrane Temperature = 1000°C, CO_2 Capture = 87.7%)

Variables	Units	Before Optimization	After Optimization	Range
Molar Flow rate of AIRREST	kmol/s	7.66	7.18	[4.5-13.5]
Molar flow rate of AIRMCM	kmol/s	37.34	39.51	[15-55]
Molar Flow rate of AFTRMETH	kmol/s	.160	.156	[0-1]
Split fraction of Split 2 (BLDPROP)		0.127	0.127	[.1-.2]
Split fraction of Split 3 (Stream2)		0.459	0.652	[.1-.7]
Air Outlet Temperature of LHEX	K	973	968	[873-985]
Air Outlet Temperature of BHEX	K	1463	1463	[1200-1500]
Efficiency contribution $\left(\frac{\text{Power output from top cycle}}{\text{Heating valuex Fuel Flow rate}}\right)$		26.5%	28%	

Table A.2: Results of Optimization of Bottoming cycle (Membrane Temperature = 1000°C, CO_2 Capture = 87.7%)

Variables	Units	Before Optimization	After Optimization	Range
Outlet Pressure of HPPMP	bar	100	100	[75-105]
Outlet Pressure of IPPMP	bar	25	25.3	[20-40]
Outlet Pressure of LPPMP	bar	5	5.5	[3-10]
Outlet Pressure of CONDPUMP	bar	0.2	0.19	[.15-.3]
Split fraction of Split 5 (LPFW)		0.152	0.184	[.1-.9]
Split fraction of Split 5 (LPIPFW)		0.083	0.166	[.08-.2]
Split fraction of Split 6 (Stream 30)		0.3	0.277	[.1-.4]
Split fraction of Split 5 (Stream 33)		0.95	0.948	[.8-1]
Outlet Temperature of air from HRSG (EXHEXIT)	K	400	376	
Outlet Temperature of steam from HRSG to HPST (HPSTM)	K	773	794	
Outlet Temperature of steam from HRSG to IPST (IPSTM)	K	773	794	
Efficiency contribution $\left(\frac{\text{Power output from bottoming cycle}}{\text{Heating valuex Fuel Flow rate}}\right)$		23%	23.6%	

Table A.3: Summary of Optimization of Top and Bottoming cycle (Membrane Temperature = 1000°C, CO_2 Capture = 87.7%)

Efficiency contribution	Before Optimization	After Optimization	Increment in % points
Top Cycle	26.5%	28%	1.5
Bottoming Cycle	23%	23.6%	0.6
Power Plant	49.5%	51.6%	2.1

A.2 Membrane Temperature = 1000°C, CO_2 Capture = 83.3%, Fuel Ratio = $\frac{\text{Fuel to "AFTERBURNER"}}{\text{Fuel to "COMBUSTOR"}} = 20$

Table A.4: Results of Optimization of Top cycle (Membrane Temperature = 1000°C, CO_2 Capture = 83.3%)

Variables	Units	Before Optimization	After Optimization	Range
Molar Flow rate of AIRREST	kmol/s	7.66	8.2	[4.5-13.5]
Molar flow rate of AIRMCM	kmol/s	37.3	39.1	[15-55]
Molar Flow rate of AFTRMETH	kmol/s	.23	.24	[0-1]
Split fraction of Split 2 (BLDPROP)		0.127	0.127	[.1-.2]
Split fraction of Split 3 (Stream2)		0.459	0.612	[.1-.7]
Air Outlet Temperature of LHEX	K	973	982	[873-985]
Air Outlet Temperature of BHEX	K	1463	1463	[1200-1500]
Efficiency contribution $\left(\frac{\text{Power output from top cycle}}{\text{Heating valuex Fuel Flow rate}}\right)$		27.4%	28.7%	

Table A.5: Results of Optimization of Bottoming cycle (Membrane Temperature = 1000°C, CO_2 Capture = 83.3%)

Variables	Units	Before Optimization	After Optimization	Range
Outlet Pressure of HPPMP	bar	100	100	[75-105]
Outlet Pressure of IPPMP	bar	25	25.7	[20-40]
Outlet Pressure of LPPMP	bar	5	5.46	[3-10]
Outlet Pressure of CONDPUMP	bar	0.2	0.19	[.15-.3]
Split fraction of Split 5 (LPFW)		0.152	0.175	[.1-.9]
Split fraction of Split 5 (LPIPFW)		0.083	0.157	[.08-.2]
Split fraction of Split 6 (Stream 30)		0.3	0.29	[.1-.4]
Split fraction of Split 5 (Stream 33)		0.95	0.947	[.8-1]
Outlet Temperature of air from HRSG (EXHEXIT)	K	399	374	
Outlet Temperature of steam from HRSG to HPST (HPSTM)	K	773	814	
Outlet Temperature of steam from HRSG to IPST (IPSTM)	K	773	814	
Efficiency contribution $\left(\frac{\text{Power output from bottoming cycle}}{\text{Heating value} \times \text{Fuel Flow rate}}\right)$		23%	23.8%	

Table A.6: Summary of Optimization of Top and Bottoming cycle (Membrane Temperature = 1000°C, CO_2 Capture = 83.3%)

Efficiency contribution	Before Optimization	After Optimization	Increment in % points
Top Cycle	27.4%	28.7%	1.2
Bottoming Cycle	23%	23.8%	0.8
Power Plant	50.4%	52.5%	2

A.3 Membrane Temperature = 1000°C, CO_2 Capture = 72%, Fuel Ratio = $\frac{\text{Fuel to "AFTERBURNER"}}{\text{Fuel to "COMBUSTOR"}} = 38.9$

Table A.7: Results of Optimization of Top cycle (Membrane Temperature = 1000°C, CO_2 Capture = 72%)

Variables	Units	Before Optimization	After Optimization	Range
Molar Flow rate of AIRREST	kmol/s	7.66	9.52	[4.5-11.5]
Molar flow rate of AIRMCM	kmol/s	37.3	38.8	[15-55]
Molar Flow rate of AFTRMETH	kmol/s	.431	.463	[0-1]
Split fraction of Split 2 (BLDPROP)		0.127	0.127	[.1-.2]
Split fraction of Split 3 (Stream2)		0.459	0.524	[.1-.7]
Air Outlet Temperature of LHEX	K	973	982	[873-985]
Air Outlet Temperature of BHEX	K	1463	1463	[1200-1500]
Efficiency contribution $\left(\frac{\text{Power output from top cycle}}{\text{Heating value} \times \text{Fuel Flow rate}}\right)$		29.6%	30.5%	

Table A.8: Results of Optimization of Bottoming cycle (Membrane Temperature = 1000°C, CO_2 Capture = 72%)

Variables	Units	Before Optimization	After Optimization	Range
Outlet Pressure of HPPMP	bar	100	100	[75-105]
Outlet Pressure of IPPMP	bar	25	25.9	[20-40]
Outlet Pressure of LPPMP	bar	5	5.56	[3-10]
Outlet Pressure of CONDPUMP	bar	0.2	0.194	[.15-.3]
Split fraction of Split 5 (LPFW)		0.152	0.154	[.1-.9]
Split fraction of Split 5 (LPIPFW)		0.083	0.164	[.08-.2]
Split fraction of Split 6 (Stream 30)		0.3	0.194	[.1-.4]
Split fraction of Split 5 (Stream 33)		0.95	0.947	[.8-1]
Outlet Temperature of air from HRSG (EXHEXIT)	K	388	381	
Outlet Temperature of steam from HRSG to HPST (HPSTM)	K	733	776	
Outlet Temperature of steam from HRSG to IPST (IPSTM)	K	733	758	
Efficiency contribution $\left(\frac{\text{Power output from bottoming cycle}}{\text{Heating valuex Fuel Flow rate}}\right)$		22.7%	24	

Table A.9: Summary of Optimization of Top and Bottoming cycle (Membrane Temperature = 1000°C, CO_2 Capture = 72%)

Efficiency contribution	Before Optimization	After Optimization	Increment in % points
Top Cycle	29.6%	30.5%	0.9
Bottoming Cycle	22.7%	24%	1.3
Power Plant	52.3%	54.5%	2.2

A.4 Membrane Temperature = 900°C, CO_2 Capture = 100%, Fuel Ratio = $\frac{\text{Fuel to "AFTERBURNER"}}{\text{Fuel to "COMBUSTOR"}} = 0$

Table A.10: Results of Optimization of Top cycle (Membrane Temperature = 900°C, CO_2 Capture = 100%)

Variables	Units	Before Optimization	After Optimization	Range
Molar Flow rate of AIRREST	kmol/s	4.04	3.21	[0-8]
Molar flow rate of AIRMCM	kmol/s	17	17.9	[10-23]
Split fraction of Split 2 (BLDPROP)		0.126	0.125	[.1-.2]
Split fraction of Split 3 (Stream2)		0.522	0.714	[.1-.9]
Air Outlet Temperature of LHEX	K	973	973	[873-985]
Air Outlet Temperature of BHEX	K	1463	1463	[1200-1500]
Efficiency contribution $\left(\frac{\text{Power output from top cycle}}{\text{Heating valuex Fuel Flow rate}}\right)$		25.5%	26.6%	

Table A.11: Results of Optimization of Bottoming cycle (Membrane Temperature = 900°C, CO_2 Capture = 100%)

Variables	Units	Before Optimization	After Optimization	Range
Outlet Pressure of HPPMP	bar	100	106	[75-108]
Outlet Pressure of IPPMP	bar	25	25.6	[20-40]
Outlet Pressure of LPPMP	bar	5	5.36	[3-10]
Outlet Pressure of CONDPUMP	bar	0.21	0.2	[.15-.3]
Split fraction of Split 5 (LPFW)		0.152	0.175	[.1-.9]
Split fraction of Split 5 (LPIPFW)		0.15	0.166	[.08-.2]
Split fraction of Split 6 (Stream 30)		0.3	0.278	[.1-.4]
Split fraction of Split 5 (Stream 33)		0.95	0.948	[.8-1]
Outlet Temperature of air from HRSG (EXHEXIT)	K	387.8	386	
Outlet Temperature of steam from HRSG to HPST (HPSTM)	K	733	754	
Outlet Temperature of steam from HRSG to IPST (IPSTM)	K	733	754	
Efficiency contribution $\left(\frac{\text{Power output from bottoming cycle}}{\text{Heating valuex Fuel Flow rate}}\right)$		22%	23.5%	

Table A.12: Summary of Optimization of Top and Bottoming cycle (Membrane Temperature = 900°C, CO_2 Capture = 100%)

Efficiency contribution	Before Optimization	After Optimization	Increment in % points
Top Cycle	25.4%	26.6%	1.2
Bottoming Cycle	22%	23.5%	1.5
Power Plant	47.4%	50.1%	2.7

A.5 Membrane Temperature = 900°C, CO_2 Capture = 90.9%, Fuel Ratio = $\frac{\text{Fuel to "AFTERBURNER"}}{\text{Fuel to "COMBUSTOR"}} = 10$

Table A.13: Results of Optimization of Top cycle (Membrane Temperature = 900°C, CO_2 Capture = 90.9%)

Variables	Units	Before Optimization	After Optimization	Range
Molar Flow rate of AIRREST	kmol/s	4.04	3.49	[0-8]
Molar flow rate of AIRMCM	kmol/s	17	16.7	[10-23]
Molar Flow rate of AFTRMETH	kmol/s	.054	.054	[0-1]
Split fraction of Split 2 (BLDPROP)		0.127	0.125	[.1-.2]
Split fraction of Split 3 (Stream2)		0.522	0.647	[.1-.9]
Air Outlet Temperature of LHEX	K	973	956	[873-985]
Air Outlet Temperature of BHEX	K	1463	1463	[1200-1500]
Efficiency contribution $\left(\frac{\text{Power output from top cycle}}{\text{Heating value} \times \text{Fuel Flow rate}}\right)$		27.3%	28.1%	

Table A.14: Results of Optimization of Bottoming cycle (Membrane Temperature = 900°C, CO_2 Capture = 90.9%)

Variables	Units	Before Optimization	After Optimization	Range
Outlet Pressure of HPPMP	bar	100	101.5	[75-108]
Outlet Pressure of IPPMP	bar	25	25.9	[20-40]
Outlet Pressure of LPPMP	bar	5	5.44	[3-10]
Outlet Pressure of CONDPUMP	bar	0.2	0.19	[.15-.3]
Split fraction of Split 5 (LPFW)		0.152	0.187	[.1-.9]
Split fraction of Split 5 (LPIPFW)		0.15	0.156	[.08-.2]
Split fraction of Split 6 (Stream 30)		0.3	0.29	[.1-.4]
Split fraction of Split 5 (Stream 33)		0.95	0.948	[.8-1]
Outlet Temperature of air from HRSG (EXHEXIT)	K	398	378	
Outlet Temperature of steam from HRSG to HPST (HPSTM)	K	773	800	
Outlet Temperature of steam from HRSG to IPST (IPSTM)	K	773	800	
Efficiency contribution $\left(\frac{\text{Power output from bottoming cycle}}{\text{Heating valuex Fuel Flow rate}}\right)$		22%	23.7%	

Table A.15: Summary of Optimization of Top and Bottoming cycle (Membrane Temperature = 900°C, CO_2 Capture = 90.9%)

Efficiency contribution	Before Optimization	After Optimization	Increment in % points
Top Cycle	27.3%	28.1%	.8
Bottoming Cycle	22%	23.7%	1.7
Power Plant	49.3%	51.8%	2.5

A.6 Membrane Temperature = 900°C, CO_2 Capture = 83.3%, Fuel Ratio = $\frac{\text{Fuel to "AFTERBURNER"}}{\text{Fuel to "COMBUSTOR"}} = 20$

Table A.16: Results of Optimization of Top cycle (Membrane Temperature = 900°C, CO_2 Capture = 83.3%)

Variables	Units	Before Optimization	After Optimization	Range
Molar Flow rate of AIRREST	kmol/s	4.04	3.7	[0-8]
Molar flow rate of AIRMCM	kmol/s	17	16.8	[10-23]
Molar Flow rate of AFTRMETH	kmol/s	.108	.108	[0-1]
Split fraction of Split 2 (BLDPROP)		0.127	0.126	[.1-.2]
Split fraction of Split 3 (Stream2)		0.522	0.587	[.1-.9]
Air Outlet Temperature of LHEX	K	973	969	[873-985]
Air Outlet Temperature of BHEX	K	1463	1463	[1200-1500]
Efficiency contribution $\left(\frac{\text{Power output from top cycle}}{\text{Heating value} \times \text{Fuel Flow rate}}\right)$		28.7%	29.1%	

Table A.17: Results of Optimization of Bottoming cycle (Membrane Temperature = 900°C, CO_2 Capture = 83.3%)

Variables	Units	Before Optimization	After Optimization	Range
Outlet Pressure of HPPMP	bar	100	101	[75-108]
Outlet Pressure of IPPMP	bar	25	25.4	[20-40]
Outlet Pressure of LPPMP	bar	5	5.46	[3-10]
Outlet Pressure of CONDPUMP	bar	0.203	0.193	[.15-.3]
Split fraction of Split 5 (LPFW)		0.152	0.175	[.1-.9]
Split fraction of Split 5 (LPIPFW)		0.15	0.157	[.08-.2]
Split fraction of Split 6 (Stream 30)		0.3	0.284	[.1-.4]
Split fraction of Split 5 (Stream 33)		0.95	0.949	[.8-1]
Outlet Temperature of air from HRSG (EXHEXIT)	K	396	371	
Outlet Temperature of steam from HRSG to HPST (HPSTM)	K	773	825	
Outlet Temperature of steam from HRSG to IPST (IPSTM)	K	773	825	
Efficiency contribution $\left(\frac{\text{Power output from bottoming cycle}}{\text{Heating valuex Fuel Flow rate}}\right)$		22%	23.9%	

Table A.18: Summary of Optimization of Top and Bottoming cycle (Membrane Temperature = 900°C, CO_2 Capture = 83.3%)

Efficiency contribution	Before Optimization	After Optimization	Increment in % points
Top Cycle	28.7%	29.1%	.4
Bottoming Cycle	22%	23.9%	1.9
Power Plant	50.7%	53%	2.3

A.7 Membrane Temperature = 900°C, CO_2 Capture = 75.2%, Fuel Ratio = $\frac{\text{Fuel to "AFTERBURNER"}}{\text{Fuel to "COMBUSTOR"}} = 33$

Table A.19: Results of Optimization of Top cycle (Membrane Temperature = 900°C, CO_2 Capture = 75.2%)

Variables	Units	Before Optimization	After Optimization	Range
Molar Flow rate of AIRREST	kmol/s	4.04	4.32	[0-8]
Molar flow rate of AIRMCM	kmol/s	17	17.2	[10-23]
Molar Flow rate of AFTRMETH	kmol/s	.179	.183	[0-1]
Split fraction of Split 2 (BLDPROP)		0.127	0.126	[.1-.2]
Split fraction of Split 3 (Stream2)		0.522	0.533	[.1-.9]
Air Outlet Temperature of LHEX	K	973	969	[873-985]
Air Outlet Temperature of BHEX	K	1463	1463	[1200-1500]
Efficiency contribution $\left(\frac{\text{Power output from top cycle}}{\text{Heating valuex Fuel Flow rate}}\right)$		30.3%	30.5%	

Table A.20: Results of Optimization of Bottoming cycle (Membrane Temperature = 900°C, CO_2 Capture = 75.2%)

Variables	Units	Before Optimization	After Optimization	Range
Outlet Pressure of HPPMP	bar	100	102	[75-108]
Outlet Pressure of IPPMP	bar	25	24.5	[20-40]
Outlet Pressure of LPPMP	bar	5	5.56	[3-10]
Outlet Pressure of CONDPUMP	bar	0.203	0.181	[.15-.3]
Split fraction of Split 5 (LPFW)		0.152	0.160	[.1-.9]
Split fraction of Split 5 (LPIPFW)		0.15	0.166	[.08-.2]
Split fraction of Split 6 (Stream 30)		0.3	0.253	[.1-.4]
Split fraction of Split 5 (Stream 33)		0.95	0.947	[.8-1]
Outlet Temperature of air from HRSG (EXHEXIT)	K	396	370	
Outlet Temperature of steam from HRSG to HPST (HPSTM)	K	773	861	
Outlet Temperature of steam from HRSG to IPST (IPSTM)	K	773	861	
Efficiency contribution $\left(\frac{\text{Power output from bottoming cycle}}{\text{Heating valuex Fuel Flow rate}}\right)$		22%	24%	

Table A.21: Summary of Optimization of Top and Bottoming cycle (Membrane Temperature = 900°C, CO_2 Capture = 75.2%)

Efficiency contribution	Before Optimization	After Optimization	Increment in % points
Top Cycle	30.3%	30.5%	.2
Bottoming Cycle	22%	24%	2
Power Plant	52.3%	54.5%	2.2

A.8 Membrane Temperature = 1100°C, CO_2 Capture = 100%, Fuel Ratio = $\frac{\text{Fuel to "AFTERBURNER"}}{\text{Fuel to "COMBUSTOR"}} = 0$

Table A.22: Results of Optimization of Top cycle (Membrane Temperature = 1100°C, CO_2 Capture = 100%)

Variables	Units	Before Optimization	After Optimization	Range
Molar Flow rate of AIRREST	kmol/s	11	10.5	[0-19.5]
Molar flow rate of AIRMCM	kmol/s	74.5	68.1	[50-83]
Split fraction of Split 2 (BLDPROP)		0.127	0.126	[.1-.2]
Split fraction of Split 3 (Stream2)		0.284	0.792	[.1-.9]
Air Outlet Temperature of LHEX	K	973	948	[873-985]
Air Outlet Temperature of BHEX	K	1463	1463	[1200-1500]
Efficiency contribution $\left(\frac{\text{Power output from top cycle}}{\text{Heating value} \times \text{Fuel Flow rate}}\right)$		22.9%	24.7%	

Table A.23: Results of Optimization of Bottoming cycle (Membrane Temperature = 1100°C, CO_2 Capture = 100%)

Variables	Units	Before Optimization	After Optimization	Range
Outlet Pressure of HPPMP	bar	100	101	[75-108]
Outlet Pressure of IPPMP	bar	25	24.8	[20-40]
Outlet Pressure of LPPMP	bar	5	5.57	[3-10]
Outlet Pressure of CONDPUMP	bar	0.2	0.195	[.15-.3]
Split fraction of Split 5 (LPFW)		0.19	0.2	[.1-.9]
Split fraction of Split 5 (LPIPFW)		0.19	0.192	[.08-.2]
Split fraction of Split 6 (Stream 30)		0.3	0.285	[.1-.4]
Split fraction of Split 5 (Stream 33)		0.95	0.947	[.8-1]
Outlet Temperature of air from HRSG (EXHEXIT)	K	398	392	
Outlet Temperature of steam from HRSG to HPST (HPSTM)	K	720	747	
Outlet Temperature of steam from HRSG to IPST (IPSTM)	K	720	747	
Efficiency contribution $\left(\frac{\text{Power output from bottoming cycle}}{\text{Heating valuex Fuel Flow rate}}\right)$		22%	22.9%	

Table A.24: Summary of Optimization of Top and Bottoming cycle (Membrane Temperature = 1100°C, CO_2 Capture = 100%)

Efficiency contribution	Before Optimization	After Optimization	Increment in % points
Top Cycle	22.9%	24.7%	1.8
Bottoming Cycle	22%	22.9%	.9
Power Plant	45%	47.5%	2.7

A.9 Membrane Temperature = 1100°C, CO_2 Capture = 90.1%, Fuel Ratio = $\frac{\text{Fuel to "AFTERBURNER"}}{\text{Fuel to "COMBUSTOR"}} = 11$

Table A.25: Results of Optimization of Top cycle (Membrane Temperature = 1100°C, CO_2 Capture = 90.1%)

Variables	Units	Before Optimization	After Optimization	Range
Molar Flow rate of AIRREST	kmol/s	11	9.86	[0-19.5]
Molar flow rate of AIRMCM	kmol/s	74.5	59.9	[50-83]
Molar Flow rate of AFTRMETH	kmol/s	.24	.187	[0-2]
Split fraction of Split 2 (BLDPROP)		0.127	0.126	[.1-.2]
Split fraction of Split 3 (Stream2)		0.284	0.7	[.1-.9]
Air Outlet Temperature of LHEX	K	973	920	[873-985]
Air Outlet Temperature of BHEX	K	1463	1463	[1200-1500]
Efficiency contribution $\left(\frac{\text{Power output from top cycle}}{\text{Heating value} \times \text{Fuel Flow rate}}\right)$		24.8%	26.4%	

Table A.26: Results of Optimization of Bottoming cycle (Membrane Temperature = 1100°C, CO_2 Capture = 90.1%)

Variables	Units	Before Optimization	After Optimization	Range
Outlet Pressure of HPPMP	bar	100	101.5	[75-108]
Outlet Pressure of IPPMP	bar	25	25.9	[20-40]
Outlet Pressure of LPPMP	bar	5	5.44	[3-10]
Outlet Pressure of CONDPUMP	bar	0.2	0.197	[.15-.3]
Split fraction of Split 5 (LPFW)		0.19	0.189	[.1-.9]
Split fraction of Split 5 (LPIPFW)		0.19	0.156	[.08-.2]
Split fraction of Split 6 (Stream 30)		0.3	0.289	[.1-.4]
Split fraction of Split 5 (Stream 33)		0.95	0.948	[.8-1]
Outlet Temperature of air from HRSG (EXHEXIT)	K	396	378	
Outlet Temperature of steam from HRSG to HPST (HPSTM)	K	750	800	
Outlet Temperature of steam from HRSG to IPST (IPSTM)	K	750	800	
Efficiency contribution $\left(\frac{\text{Power output from bottoming cycle}}{\text{Heating valuex Fuel Flow rate}}\right)$		22.5%	22.6%	

Table A.27: Summary of Optimization of Top and Bottoming cycle (Membrane Temperature = 1100°C, CO_2 Capture = 90.1%)

Efficiency contribution	Before Optimization	After Optimization	Increment in % points
Top Cycle	25.8%	27.7%	1.9
Bottoming Cycle	23.1%	23.2%	.1
Power Plant	48.9%	50.9%	2

A.10 Membrane Temperature = 1100°C, CO_2 Capture = 83.3%, Fuel Ratio = $\frac{\text{Fuel to "AFTERBURNER"}}{\text{Fuel to "COMBUSTOR"}} = 20$

Table A.28: Results of Optimization of Top cycle (Membrane Temperature = 1100°C, CO_2 Capture = 83.3%)

Variables	Units	Before Optimization	After Optimization	Range
Molar Flow rate of AIRREST	kmol/s	11	11.7	[0-19.5]
Molar flow rate of AIRMCM	kmol/s	74.5	62.3	[50-83]
Molar Flow rate of AFTRMETH	kmol/s	.435	.359	[0-2]
Split fraction of Split 2 (BLDPROP)		0.127	0.126	[.1-.2]
Split fraction of Split 3 (Stream2)		0.284	0.643	[.1-.9]
Air Outlet Temperature of LHEX	K	973	929	[873-985]
Air Outlet Temperature of BHEX	K	1463	1463	[1200-1500]
Efficiency contribution $\left(\frac{\text{Power output from top cycle}}{\text{Heating value} \times \text{Fuel Flow rate}}\right)$		26.8%	28.7%	

Table A.29: Results of Optimization of Bottoming cycle (Membrane Temperature = 1100°C, CO_2 Capture = 83.3%)

Variables	Units	Before Optimization	After Optimization	Range
Outlet Pressure of HPPMP	bar	100	101	[75-108]
Outlet Pressure of IPPMP	bar	25	26.2	[20-40]
Outlet Pressure of LPPMP	bar	5	5.62	[3-10]
Outlet Pressure of CONDPUMP	bar	0.2	0.199	[.15-.3]
Split fraction of Split 5 (LPFW)		0.19	0.177	[.1-.9]
Split fraction of Split 5 (LPIPFW)		0.19	0.148	[.08-.2]
Split fraction of Split 6 (Stream 30)		0.3	0.316	[.1-.4]
Split fraction of Split 5 (Stream 33)		0.95	0.94	[.8-1]
Outlet Temperature of air from HRSG (EXHEXIT)	K	393.3	388	
Outlet Temperature of steam from HRSG to HPST (HPSTM)	K	773	793	
Outlet Temperature of steam from HRSG to IPST (IPSTM)	K	773	793	
Efficiency contribution $\left(\frac{\text{Power output from bottoming cycle}}{\text{Heating value} \times \text{Fuel Flow rate}}\right)$		23.1%	23.2%	

Table A.30: Summary of Optimization of Top and Bottoming cycle (Membrane Temperature = 1100°C, CO_2 Capture = 83.3%)

Efficiency contribution	Before Optimization	After Optimization	Increment in % points
Top Cycle	26.8%	28.7%	1.9
Bottoming Cycle	23.1%	23.2%	.1
Power Plant	49.9%	51.9%	2

A.11 Membrane Temperature = 1100°C, CO_2 Capture = 68.6%, Fuel Ratio = $\frac{\text{Fuel to "AFTERBURNER"}}{\text{Fuel to "COMBUSTOR"}} = 45.7$

Table A.31: Results of Optimization of Top cycle (Membrane Temperature = 1100°C, CO_2 Capture = 68.6%)

Variables	Units	Before Optimization	After Optimization	Range
Molar Flow rate of AIRREST	kmol/s	11	15.6	[0-19.5]
Molar flow rate of AIRMCM	kmol/s	74.5	69.7	[50-83]
Molar Flow rate of AFTRMETH	kmol/s	.926	.925	[0-2]
Split fraction of Split 2 (BLDPROP)		0.127	0.126	[.1-.2]
Split fraction of Split 3 (Stream2)		0.284	0.496	[.1-.9]
Air Outlet Temperature of LHEX	K	973	958	[873-985]
Air Outlet Temperature of BHEX	K	1463	1463	[1200-1500]
Efficiency contribution $\left(\frac{\text{Power output from top cycle}}{\text{Heating valuex Fuel Flow rate}}\right)$		28%	29.9%	

Table A.32: Results of Optimization of Bottoming cycle (Membrane Temperature = 1100°C, CO_2 Capture = 68.6%)

Variables	Units	Before Optimization	After Optimization	Range
Outlet Pressure of HPPMP	bar	100	103	[75-108]
Outlet Pressure of IPPMP	bar	25	26.2	[20-40]
Outlet Pressure of LPPMP	bar	5	5.78	[3-10]
Outlet Pressure of CONDPUMP	bar	0.2	0.194	[.15-.3]
Split fraction of Split 5 (LPFW)		0.19	0.147	[.1-.9]
Split fraction of Split 5 (LPIPFW)		0.19	0.162	[.08-.2]
Split fraction of Split 6 (Stream 30)		0.3	0.282	[.1-.4]
Split fraction of Split 5 (Stream 33)		0.95	0.949	[.8-1]
Outlet Temperature of air from HRSG (EXHEXIT)	K	387	368	
Outlet Temperature of steam from HRSG to HPST (HPSTM)	K	778	868	
Outlet Temperature of steam from HRSG to IPST (IPSTM)	K	791	868	
Efficiency contribution $\left(\frac{\text{Power output from bottoming cycle}}{\text{Heating valuex Fuel Flow rate}}\right)$		24%	24.4%	

Table A.33: Summary of Optimization of Top and Bottoming cycle (Membrane Temperature = 1100°C, CO_2 Capture = 68.6%)

Efficiency contribution	Before Optimization	After Optimization	Increment in % points
Top Cycle	28%	29.9%	1.9
Bottoming Cycle	24%	24.4%	.4
Power Plant	52%	54.3%	2.3

Appendix B

Parabolic Trough Model

A cross section of parabolic trough receiver is shown in Figure B-1. For the sake of simplicity, the solar absorption into the glass envelope is treated as a heat flux. Though solar absorption is a heat generation phenomenon, this assumption is justified, as the solar absorption coefficient is small for glass. The solar absorption in the glass envelope is calculated using the equations

$$\dot{Q}_{\text{abs}} = qA\alpha\eta_{\text{abs}} \tag{B.1}$$

$$\eta_{\text{abs}} = \epsilon_1\epsilon_2\epsilon_3\epsilon_4\epsilon_5\epsilon_6\rho_{cl}K \tag{B.2}$$

$$K = \cos\theta + 0.000884\theta - 0.0000536\theta^2 \tag{B.3}$$

K, the incident angle modifier is needed for cases when solar rays is not normal to the collector aperture. It is a function of θ, the angle of incidence between the normal to the parabolic trough and the solar rays. η_{abs}, the effective optical efficiency of the glass envelope is the function of the optical efficiencies. A reflectivity value of 0.88 is used in the model. $\dot{Q}_{\text{abs}}$, the solar absorption in the glass envelope is calculated as a product of q, the solar irradiance, A, the projected normal reflective surface area of the collector, η_{abs}, the effective

optical efficiency of glass envelope, and α, the absorptance of the glass envelope. Table B.1 shows the specifications of parabolic trough used, including the value of each of the optical efficiency terms used in the model and their descriptions.

Figure B-2 shows a thermal resistor model of the HCE which accounts only for conduction and convection, and neglects radiation. As the selective coating has a high absorptance for radiation in the solar energy spectrum, and low emittance in the long wavelength spectrum (maximum temperature which can be attained in a parabolic trough is about 670 K), in order to reduce thermal radiation losses [72], heat transfer through radiation has been neglected in the model. Each term in the resistor model is calculated using the formulae or correlations available in Reference [4].

Conduction through the absorber pipe:

$$R_{\text{cond,pipe}} = \frac{\log \frac{D_{\text{pipe},o}}{D_{\text{pipe},i}}}{2\pi k_{\text{pipe}} L_{\text{pipe}}} \tag{B.4}$$

where $R_{\text{cond,pipe}}$ is the conduction heat transfer resistance through the receiver pipe, $D_{\text{pipe},i}$ and $D_{\text{pipe},o}$ are the inner and outer diameters of the receiver pipe, k_{pipe} is the thermal conductivity of the receiver pipe and L_{pipe} is the length of the receiver pipe.

Conduction through the glass envelope:

$$R_{\text{cond,glass}} = \frac{\log \frac{D_{\text{glass},o}}{D_{\text{glass},i}}}{2\pi k_{\text{glass}} L_{\text{pipe}}} \tag{B.5}$$

where $R_{\text{cond,glass}}$ is the conduction heat transfer resistance through the glass envelope, $D_{\text{glass},i}$ and $D_{\text{glass},o}$ are the inner and outer diameters of the glass envelope, and k_{glass} is the thermal conductivity of the glass envelope.

Convection between the outer surface of the absorber pipe and the inner surface of glass envelope which is filled with air at low-pressure [4]:

$$R_{\text{conv},a} = \frac{1}{0.24728\pi D_{\text{pipe},o} L_{\text{pipe}}} \tag{B.6}$$

where $R_{\text{conv},a}$ is the convection heat transfer resistance of air between the outer surface

of the absorber pipe and the inner surface of glass envelope.

Convection between the HTF and the inner surface of the absorber pipe:

$$R_{\text{conv},p} = \frac{1}{h\pi D_{\text{pipe},i} L_{\text{pipe}}} \tag{B.7}$$

where

$$h_{\text{HTF}} = \text{Nu}_{\text{HTF}} \cdot k_{\text{HTF}} D_{\text{pipe},i} \tag{B.8}$$

where $R_{\text{conv},p}$ is the convection heat transfer resistance of HTF inside the absorber pipe, and h_{HTF} and k_{HTF} are the heat transfer coefficient and thermal conductivity of the HTF. The Nusselt number of the HTF, Nu_{HTF}, is calculated using standard correlations. The Nusselt number is taken as 4.36 for laminar flow. Gnielinski correlation is used for turbulent flow.

Convection between the glass envelope outer surface and surroundings:

$$R_{\text{conv},g} = \frac{1}{h\pi D_{\text{glass},o} L_{\text{pipe}}} \tag{B.9}$$

where

$$h_{\text{air}} = \text{Nu}_{\text{air}} \cdot k_{\text{air}} D_{\text{glass},o} \tag{B.10}$$

where $R_{\text{conv},g}$ is the heat transfer resistance between the outer surface of the glass envelope and the surroundings, and h_{air} and k_{air} are the heat transfer coefficient and thermal conductivity of air.

The Nusselt number of air, Nu_{air}, is calculated using the Churchill and Bernstein correlation.

Based on the resistor network, the outlet HTF temperature can be calculated using the following equations:

$$\dot{m}c_p\frac{dT_B}{dx} = \frac{T_{pipe,i} - T_B}{R_{conv,p}} \tag{B.11}$$

$$\dot{Q}_{abs} = \frac{T_{pipe,i} - T_{amb}}{R_{rest}} \tag{B.12}$$

$$R_{rest} = R_{cond,pipe} + R_{cond,glass} + R_{conv,a} + R_{conv,g} \tag{B.13}$$

where $\dot{m}$ is the mass flow rate of the HTF, c_p is the heat capacity of the HTF, $T_{pipe,i}$ is the temperature of the pipe at the inner surface, and T_B is the bulk temperature of the HTF.

Discretization of Equations (B.11) and (B.12) leads to:

$$\frac{\dot{Q}_{abs}}{N} = \frac{T_{pipe,i,j} - T_{amb}}{R_{rest}} \tag{B.14}$$

$$\dot{m}c_p(T_{B,j} - T_{B,j-1}) = \frac{T_{pipe,i,j} - T_{B,j}}{R_{conv,p}} \tag{B.15}$$

where j refers to the index of the discretized element, and N is the number discretization elements.

The pressure drop is calculated using the friction factor from the Zigrang and Sylvester correlation as follows:

$$\frac{1}{\sqrt{f}} = -2\log\left[\frac{k_{pipe}}{2.7D_{pipe,i}} - \frac{5.02}{Re}\log\left(\frac{k_{pipe}}{3.7D_{pipe,i}} - \frac{5.02}{Re}\log\left(\frac{k_{pipe}}{3.7D_{pipe,i}} - \frac{13}{Re}\right)\right)\right] \tag{B.16}$$

$$\Delta P = f\frac{L_{pipe}}{D_{pipe,i}}\frac{\rho_{HTF}v_{HTF}^2}{2} \tag{B.17}$$

ΔP, the pressure drop of the HTF is calculated as a function of the friction factor, f, ρ_{HTF}, the density of the HTF, v_{HTF}, the velocity of the HTF, and the length and inner

Symbols	Description	Units	Value
ϵ_1	HCE shadowing (bellows, shielding, supports)	-	0.974
ϵ_2	Tracking error	-	0.994
ϵ_3	Geometry error (mirror alignment)	-	0.98
ϵ_4	Dirt on mirrors	-	Reflectivity/ρ_{cl}
ϵ_5	Dirt on HCE	-	$(1+\epsilon_4)/2$
ϵ_6	Unaccounted losses	-	0.96
ρ_{cl}	Clean mirror reflectance	-	0.935
T_{inf}	Surrounding temperature	K	300
k_{air}	Thermal conductivity of air	W/(m·K)	0.024
v_{wind}	Wind speed	m/s	2
Reflectivity	Reflectivity of clean mirror		.88
k_{glass}	Thermal conductivity of glass envelope	W/(m·K)	1.05
k_{pipe}	Thermal conductivity of receiver pipe	W/(m·K)	.43
$D_{\text{glass},i}$	Inner diameter of glass envelope	m	0.109
$D_{\text{glass},o}$	Outer diameter of glass envelope	m	0.115
$D_{\text{pipe},i}$	Inner diameter of receiver pipe	m	0.066
$D_{\text{pipe},o}$	Outer diameter of receiver pipe	m	0.07
α	Absorptance of receiver pipe		0.94
τ	Transmittance of glass envelope		0.935

Table B.1: Specifications of the parabolic trough used in the model [4].

diameter of the receiver pipe.

Herein, 150 parabolic troughs are considered in parallel. It is seen than for a fixed projected area, the number of troughs in parallel only affects pressure drop, i.e., other parameters such as temperature remain the same. As seen below, lowering the number of troughs in parallel leads to a greater length of the receiver pipe for each parabolic trough, resulting in a higher pressure drop. 150 parabolic troughs were chosen in parallel here to have a reasonably low-pressure drop. The difference in power output due to the pressure drop between using 50 parallel parabolic troughs and 150 parabolic troughs is about 2 MW. Since the change in the power output is not very different and the number of troughs in parallel does not affect any other parameter except pressure drop, the number of troughs chosen in parallel is not a

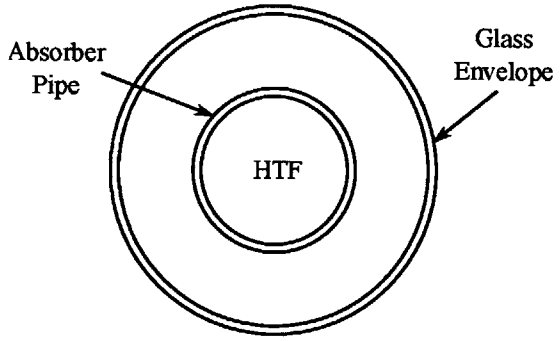

Figure B-1: Cross-section of the parabolic trough receiver.

(1) Heat Transfer Fluid
(2) Absorber Inner Surface
(3) Absorber Outer Surface
(4) Glass Envelope Inner Surface
(5) Glass Envelope Outer Surface
(6) Surroundings

Figure B-2: Thermal resistor model for a HCE.

critical parameter. The total area of the parabolic trough is found to be 3.9×10^5 (Section 3.3.3). Hence, the area of each trough is given by $3.9 \times 10^5/150 = 2.6 \times 10^3$ m^2

$$A = w \cdot L_{\text{pipe}} \tag{B.18}$$

where w is the aperture width and L_{pipe} is the length of the receiver pipe.

In the literature, the available values of the aperture width varies between 0.5 m to 11 m. Herein, the aperture width was fixed based on an LS-3 SEGS plant with aperture width = 5.76 m (in accordance to [52]) which results in a length of 450 m.

THIS PAGE INTENTIONALLY LEFT BLANK

Appendix C

Angle of Incidence Calculation

The angle of incidence is calculated using the standard formulae from the literature [70]

$$\begin{aligned}\cos\theta = \cos\beta(&\sin\delta\sin\phi + \cos\delta\cos\phi\cos\omega)\\ &- \cos\delta\sin\omega\sin\beta\sin\gamma\\ &+ \sin\beta\cos\gamma(\sin\delta\cos\phi - \cos\delta\cos\omega\sin\phi)\end{aligned} \tag{C.1}$$

where θ is the angle of incidence between the normal to the parabolic trough and the solar rays, β is the tilt angle, ϕ is the latitude of the KFUPM weather station (26.3097°N), ω is the hour angle, and δ is the declination angle. The hour and declination angles are calculated as shown below. The Local Standard Time Meridian (LSTM) is a reference meridian used for a particular time zone.

$$\text{LSTM} = 15^\circ \cdot \Delta T_{GMT} \tag{C.2}$$

ΔT_{GMT} is the difference between the local time (LT) and the Greenwich Mean Time (GMT) in hours.

The Equation of Time (EoT) is an empirical equation that corrects for the eccentricity of the earth's orbit and the earth's axial tilt.

$$\mathrm{EoT} = 9.87\sin 2B - 7.53\cos B - 1.5\sin B \tag{C.3}$$

where,

$$B = \frac{360}{365}(d - 81) \tag{C.4}$$

where d is the number of days since the start of the year.

The net time correction factor accounts for the variation of the local solar time (LST) within a given zone due to the longitudinal variations within the time zone.

$$\mathrm{TC} = 4(\mathrm{LSTM} - \mathrm{Longitude}) + \mathrm{EoT} \tag{C.5}$$

$$\mathrm{LST} = \mathrm{LT} + \frac{\mathrm{TC}}{60} \tag{C.6}$$

Hour angle converts the local solar time (LST) into the number of degrees which the sun moves across sky.

$$\omega = 15°(\mathrm{LST} - 12) \tag{C.7}$$

The declination angle, δ is calculated as shown in (C.8)

$$\delta = 23.45° \sin\left[(d - 81)\frac{360}{365}\right] \tag{C.8}$$

where d is the day of the year.

Nomenclature

A	Projected normal reflective surface area of the collector	m^2
AZEP	Advanced Zero Emissions Plant	-
c_p	Specific heat capacity	J/(kg·K)
CCGT	Combined Cycle Gas Turbine	-
CCS	Carbon Capture and Sequestration	-
CFD	Computational Fluid Dynamics	-
CST	Concentrated Solar Thermal	-
d	Day of the year	-
$D_{\text{glass},i}$	Inner diameter of glass envelope	m
$D_{\text{glass},o}$	Outer diameter of glass envelope	m
$D_{\text{pipe},i}$	Inner diameter of receiver pipe	m
$D_{\text{pipe},o}$	Outer diameter of receiver pipe	m
DNI	Direct Normal Irradiance	W/m^2
DSG	Direct Stream Generation	-
EoT	Equation of Time	-

f	Friction Factor	-
h	Heat transfer coefficient	W/(m²·K)
HCE	Heat Collector Element	-
HRSG	Heat Recovery Steam Generator	-
HTF	Heat Transfer Fluid	-
ITM	Ion Transport Membrane	-
K	Incident angle modifier	-
k	Thermal conductivity	W/(m·K)
L_{pipe}	Length of the receiver pipe	m
LHV	Lower Heating Value of fuel	MJ/kmol
LMTD	Log Mean Temperature Difference	-
LST	Local Solar Time	h
LSTM	Local Standard Time Meridian	°
LT	Local Time	h
$\dot{m}$	Mass flow rate	kg/s
$\dot{n}_{\text{fuel}}$	Mole flow rate of fuel	kmol/s
N	Number of discretization elements	-
Nu	Nusselt Number	-
$\dot{q}_{\text{DNI,nominal}}$	Nominal (taken at maximal) Direct Normal Irradiance	MW/m²
$\dot{q}_{\text{DNI}}$	Direct Normal Irradiance	MW/m²

$\dot{Q}_{\text{abs}}$	Solar absorption in glass envelope	MW
$\dot{Q}_{\text{fuel}}$	Heating rate input from the fuel	MW
$\dot{Q}_{\text{solar}}$	Solar energy transfer rate	MW
$\dot{Q}_{\text{trough,nominal}}$	Nominal heat transfer rate from the receiver pipe to the heat transfer fluid	MW
$\dot{Q}_{\text{trough}}$	Heat transfer rate from the receiver pipe to the heat transfer fluid	MW
$Q_{\text{fuel,annual}}$	Total heat input of fuel in a year	MWh
$Q_{\text{trough,annual}}$	Total heat added to the heat transfer fluid by the parabolic trough in a year	MWh
R_{a}	Heat transfer resistance of air between outer surface of the absorber pipe and inner surface of glass envelope	K/W
R_{g}	Heat transfer resistance of air between outer surface of the glass envelope and surroundings	K/W
R_{p}	Heat transfer resistance of heat transfer fluid inside the absorber pipe	K/W
Reflectivity	Reflectivity of clean mirror	-
T	Temperature	K
TC	Time correction factor	-
v	Velocity	m/s
w	Aperture width	m

$\dot{W}_{\text{AZEP+solar,ref}}$	Power output of the reference combination of AZEP + Solar plants	MW
$\dot{W}_{\text{ref}}$	Power output of the AZEP only reference plant	MW
$\dot{W}_{\text{solar}}$	Net power output of a generic solar only power plant	MW
$W_{\text{AZEP+solar,ref,annual}}$	Total work output of the reference combination of AZEP + Solar plants in a year	MWh
$W_{\text{hybrid,annual}}$	Total work output of the solar-thermal hybrid plant in a year	MWh
$X_{\text{s,i}}$	Solar share based on energy input	-

Greek Symbols

α	Absorptance of glass envelope	-
β	Tilt angle	°
δ	Declination angle	°
ϵ_1	HCE shadowing (bellows, shielding, supports)	-
ϵ_2	Tracking error	-
ϵ_3	Geometry error (mirror alignment)	-
ϵ_4	Dirt on mirrors	-
ϵ_5	Dirt on HCE	-
ϵ_6	Unaccounted losses	-
ϕ	Latitude	°
$\eta_{\text{inc-sol-annual}}$	Annual incremental solar efficiency	-
η_{ref}	Efficiency of AZEP only reference plant	-

$\eta_{\text{sol-elec,ref}}$	Solar to electrical energy efficiency of solar-thermal reference cycle	-
$\eta_{\text{sol-elec}}$	Solar to electrical energy efficiency of a generic solar-thermal cycle	-
$\eta_{\text{trough-elec,ref}}$	Concentrated solar energy to electrical energy efficiency of solar-thermal reference cycle	-
η_{abs}	Effective optical efficiency of glass envelope	-
ω	Hour angle	°
θ	Angle of incidence between the normal to the parabolic trough and the solar rays	°
ρ_{HTF}	Density of heat transfer fluid	kg/m^3
ρ_{cl}	Clean mirror reflectance	-
τ	Transmittance of glass envelope	-

Subscripts

air	Surrounding air
B	Bulk
cond	Conduction
conv	Convection
fuel	Fuel input
glass	Glass envelope
HTF	Heat Transfer Fluid
inf	Environment
j	Discretized element

pipe	Receiver pipe
solar	Solar field input
wind	Wind

Bibliography

[1] P. Schwarzbözl, R. Buck, C. Sugarmen, A. Ring, M. J. M. Crespo, P. Altwegg, and J. Enrile. Solar gas turbine systems: Design, cost and perspectives. *Solar Energy*, 80 (10):1231–1240, 2006. ISSN 0038-092X.

[2] M. J. Montes, A. Rovira, M. Munoz, and J. M. Martínez-Val. Performance analysis of an integrated solar combined cycle using direct steam generation in parabolic trough collectors. *Applied Energy*, 88(9):3228–3238, 2011. ISSN 0306-2619.

[3] E. J. Sheu and A. Mitsos. Optimization of a hybrid solar-fossil fuel plant: Solar steam reforming of methane in a combined cycle. *Energy*, 51:193–202, 2013.

[4] R. Forristall. Heat transfer analysis and modeling of a parabolic trough solar receiver implemented in engineering equation solver. Technical report, National Renewable Energy Laboratory, Colorado, October 2003.

[5] International Energy Agency. CO_2 Emissions From Fuel Combustion. *IEA Statistics*, 2009.

[6] T. F. Wall. Combustion processes for carbon capture. In *Proceedings of the Combustion Institute*, pages 31–47, 2007.

[7] A. P. Simpson and A. J. Simon. Second law comparison of oxy-fuel combustion and post-combustion carbon dioxide separation. *Energy Conversion and Management*, 48 (11):3034–3045, 2007. ISSN 0196-8904.

[8] R. Steeneveldt, B. Berger, and T. A. Torp. CO_2 capture and storage: Closing the knowing-doing gap. *Chemical Engineering Research and Design*, 84(9):739–763, 2006. ISSN 0263-8762.

[9] M. A. Habib, H. M. Badr, S. F. Ahmed, R. Ben-Mansour, K. Mezghani, S. Imashuku, G. J. la O', Y. Shao-Horn, N. D. Mancini, A. Mitsos, P. Kirchen, and A. F. Ghoneim. A review of recent developments in carbon capture utilizing oxy-fuel combustion in conventional and ion transport membrane systems. *International Journal of Energy Research*, 35(9):741–764, 2011.

[10] H. Zebian, M. Gazzino, and A. Mitsos. Multi-variable optimization of pressurized oxy-coal combustion. *Energy*, 38(1):37–57, 2012.

[11] H. Zebian, N. Rossi, M. Gazzino, D. Cumbo, and A. Mitsos. Optimal design and operation of pressurized oxy-coal combustion with a direct contact separation column. *Energy*, 49:268–278, 2013.

[12] H. Zebian and A. Mitsos. Pressurized Oxy-Coal Combustion: Ideally Flexible to Uncertainties. *Submitted*, 11 November 2012.

[13] H. Zebian and A. Mitsos. Pressurized OCC Process Ideally Flexible to The Thermal Load. *To be submitted*, May 2013.

[14] I. Pfaff and A. Kather. Comparative thermodynamic analysis and integration issues of CCS steam power plants based on oxy-combustion with cryogenic or membrane based air separation. In *Proceedings of the 9th International Conference on Greenhouse Gas Control Technologies (GHGT-9)*, pages 495–502, Washington DC, USA, 2009.

[15] P. J. Gellings and H. M. Bouwmeester. *The CRC handbook of solid state electrochemistry*. CRC press, 1997.

[16] S. Sundkvist, S. Julsrud, B. Vigeland, T. Naas, M. Budd, H. Leistner, and D. Winkler. Development and testing of AZEP reactor components. In *8th International Conference on Greenhouse Gas Control Technologies (GHGT-8)*, pages 180–187, 2007.

[17] S. J. Xu and W. J. Thomson. Oxygen permeation rates through ion-conducting perovskite membranes. *Chemical Engineering Science*, 54(17):3839–3850, 1999. ISSN 0009-2509.

[18] J. Sunarso, S. Baumann, J. M. Serra, W. A. Meulenberg, S. Liu, Y. S. Lin, and J. C. Diniz da Costa. Mixed ionic-electronic conducting (MIEC) ceramic-based membranes for oxygen separation. *Journal of Membrane Science*, 320(1-2):13–41, 2008. ISSN 0376-7388.

[19] B. A. van Hassel. Oxygen transfer across composite oxygen transport membranes. *Solid State Ionics*, 174(1-4):253–260, 2004. ISSN 0167-2738.

[20] N. D. Mancini and A. Mitsos. Conceptual Design and Analysis of ITM Oxy-combustion Power Cycles. *Phys. Chem. Chem. Phys.*, 13:21351–21361, 2011.

[21] N. D. Mancini, S. Gunasekaran, and A. Mitsos. A Multiple-Compartment Ion-Transport-Membrane Reactive Oxygen Separator. *Industrial & Engineering Chemistry Research*, 51(23):7988–7997, 2012.

[22] N. D. Mancini and A. Mitsos. Ion Transport Membranes for Oxy-combustion – Part II: Analysis and Comparison of Alternatives. *Energy*, 36(8):4721–4739, 2011. ISSN 0360-5442.

[23] N. D. Mancini and A. Mitsos. Ion Transport Membranes for Oxy-combustion – Part I: Intermediate-Fidelity Modeling. *Energy*, 36(8):4701–4720, 2011. ISSN 0360-5442.

[24] Numerica Technology, JACOBIAN Modeling and Optimization Software. `http://www.numericatech.com`, 2009.

[25] H. Kvamsdal, K. Jordal, and O. Bolland. A quantitative comparison of gas turbine cycles with CO_2 capture. *Energy*, 32(1):10–24, 2007. ISSN 0360-5442.

[26] R. Anantharaman, O. Bolland, and K. Asen. Novel cycles for power generation with CO_2 capture using OMCM technology. *Energy Procedia*, 1:335–342, 2009.

[27] K. E. Colombo, O. Bolland, V. V. Kharton, and C. Stiller. Simulation of an oxygen membrane-based combined cycle power plant: part-load operation with operational and material constraints. *Energy Environ. Sci.*, 2(12):1310–1324, 2009.

[28] K. E. Colombo and O. Bolland. Dynamic simulation of an oxygen mixed conducting membrane-based gas turbine power cycle for CO_2 capture. *Energy Procedia*, 1:431–438, 2009.

[29] C. K. Eichhorn, I. Lars, B. Olav, and H. Svein. Dynamic modelling of an oxygen mixed conducting membrane and model reduction for control. *Journal of Membrane Science*, 336(1-2):50–60, 2009.

[30] E. Yantovski, J. Gorski, B. Smyth, and J. Elshof. Zero-emission fuel-fired power plants with ion transport membrane. *Energy*, 29(12-15):2077–2088, 2004. ISSN 0360-5442.

[31] K. Foy and J. McGovern. Analysis of the effects of combining air separation with combustion in a zero emissions (ZEITMOP) cycle. *Energy Conversion and Management*, 48(11):3046–3052, 2007.

[32] D. Fiaschi, F. Gamberi, M. Bartlett, and T. Griffin. The air membrane-ATR integrated gas turbine power cycle: A method for producing electricity with low CO_2 emissions. *Energy Conversion and Management*, 46(15-16):2514–2529, 2005.

[33] P. P. Walsh. and P. Fletcher. *Gas turbine performance*. Blackwell Science 2004, 2004.

[34] D. P. Bertsekas. *Nonlinear Programming*. Athena Scientific, 1999.

[35] S. Gunasekaran, N. D. Mancini, and A. Mitsos. Design and Optimization of ITM Oxy-Combustion Power Plants. In *Proceedings of ECOS 2012*, Perugia, Italy, 2012.

[36] E. J. Sheu, A. Mitsos, A. E. Eter, M. A. E. Mokheimer, M. A. Habib, and A. Al-Qutub. A review of hybrid solar-fossil fuel power generation systems and performance metrics. *Journal of Solar Energy Engineering*, 134(4):041006–041022, 2012.

[37] S. Liu and G. R. Gavalas. Oxygen selective ceramic hollow fiber membranes. *Journal of Membrane Science*, 246(1):103–108, 2005. ISSN 0376-7388.

[38] E. Yantovski, M. Shokotov, V. Shokotov, J. McGovern, and K. Foy. Elaboration of Zero Emissions Membrane Piston Engine System (ZEMPES) for Propane Fuelling. In *Proceedings of Fourth Annual Conference on Carbon Capture and Sequestration*, 2005.

[39] D. J. Dillon, R. S. Panesar, R. A. Wall, R. J. Allam, V. White, J. Gibbins, and M. R. Haines. Oxy-combustion processes for CO2 capture from advanced supercritical PF and NGCC power plant. In E. S. Rubin, D. W. Keith, C. F. Gilboy, M. Wilson, T. Morris, J. Gale, and K. Thambimuthu, editors, *Greenhouse Gas Control Technologies 7*, pages 211–220. Elsevier Science Ltd, Oxford, 2005.

[40] G. Lozza, M. Romano, and A. Giuffrida. Thermodynamic performance of igcc with oxy-combustion CO_2 capture. In *First International Conference on Sustainable Fossil Fuels for Future Energy - S4FE 2009*, 2009.

[41] C. Gou, R. Cai, and H. Hong. A novel hybrid oxy-fuel power cycle utilizing solar thermal energy. *Energy*, 32:1707–1714, 2007.

[42] X. Tan, Z. Wang, B. Meng, X. Meng, and K. Li. Pilot Scale Production of Oxygen from Air Using Perovskite Hollow Fiber Membranes. *Journal of Membrane Science*, 352:189–196, 2010.

[43] E. Walker, Michael, Abbasian, Javad, Chmielewski, J. Donald, Castaldi, and J. Marco. Dry Gasification Oxy-combustion Power Cycle. *Energy & Fuels*, 25(5):2258–2266, 2011.

[44] F. Petrakopoulou, G. Tsatsaronis, and T. Morosuk. Exergoeconomic analysis of an advanced zero emission plant. *Journal of Engineering for Gas Turbines and Power-Transactions of the Asme*, 133(11), 2011.

[45] H. Price, E. Lüpfert, D. Kearney, E. Zarza, G. Cohen, R. Gee, and R. Mahoney. Advances in parabolic trough solar power technology. *Journal of Solar Energy Engineering*, 124(2):109–125, 2002.

[46] E. A. de Meo and J. F. Galdo. Renewable energy technology characterizations. Technical report, Electric Power Research Institute (EPRI) and U.S. Department of Energy, Washington, D. C., December 1997.

[47] M. Horn, H. Führing, and J. Rheinländer. Economic analysis of integrated solar combined cycle power plants: A sample case: The economic feasibility of an ISCCS power plant in Egypt. *Energy*, 29:935–945, 2004. ISSN 0360-5442.

[48] F. Cavallaro. Multi-criteria decision aid to assess concentrated solar thermal technologies. *Renewable Energy*, 34(7):1678–1685, 2009. ISSN 0960-1481.

[49] R. Buck, M. Abele, J. Kunberger, T. Denk, P. Heller, and E. Lüpfert. Receiver for solar-hybrid gas turbine and combined cycle systems. *J. Phys. IV France*, 09:Pr3–537–Pr3–544, 1999.

[50] M. Romero, R. Buck, J. Kunberger, and J. E. Pacheco. An update on solar central receiver systems, projects and technologies. *Journal of Solar Energy Engineering*, 124 (2):98–108, April 2002.

[51] A. Baghernejad and M. Yaghoubi. Exergy analysis of an integrated solar combined cycle system. *Renewable Energy*, 35(10):2157 – 2164, 2010. ISSN 0960-1481.

[52] S. R. Cable. Solar Trough Generation. In *ASES Forum*, Washington DC, 2001.

[53] M. Günther, M. Joemann, and S. Csambor. Advanced CST teaching materials. chapter Parabolic Trough Technology. enerMENA, 2011. URL `http://www.iresen.org/energyscience/bibliotheque/cours/1361468741Chapter05parabolictrough.pdf`.

[54] S. P. Sukhatme and J. K. Nayak. *Solar Energy: Principles of Thermal Collection and Storage*. McGraw-Hill, 2008.

[55] J. Birnbaum, M. Eck, M. Fichtner, T. Hirsch, D. Lehmann, and G. Zimmermann. A direct steam generation solar power plant with integrated thermal storage. *Journal of Solar Energy Engineering*, 132(3):031014–031019, 2010.

[56] E. Zarza, M. E. Rojas, L. González, J. M. Caballero, and F. Rueda. INDITEP: The first pre-commercial DSG solar power plant. *Solar Energy*, 80(10):1270–1276, 2006. ISSN 0038-092X.

[57] M. Silva, M. Blanco, and V. Ruiz. Integration of solar thermal energy in a conventional power plant : The colón solar project. *J. Phys. IV France*, 09:Pr3–189–Pr3–194, 1999.

[58] Y. Yang, Y. Cui, H. Hou, X. Guo, Z. Yang, and N. Wang. Research on solar aided coal-fired power generation system and performance analysis. *Science in China Series E: Technological Sciences*, 51(8):1211–1221, 2008. ISSN 1006-9321.

[59] N. D. Mancini. System-level design of ion transport membrane oxy-combustion power plants. Master's thesis, Massachusetts Institute of Technology, 2011.

[60] R. El-Khaja. Solar-thermal hybridization of advanced zero emissions power plants, 2012. Bachelor's thesis, Massachusetts Institute of Technology.

[61] P. S. Pak, T. Hatikawa, and Y. Suzuki. A hybrid power generation system utilizing solar thermal energy with CO2 recovery based on oxygen combustion method. *Energy Conversion and Management*, 36(69):823–826, 1995. ISSN 0196-8904.

[62] P. S. Pak, Y. Suzuki, and T. Kosugi. A CO2-capturing hybrid power-generation system with highly efficient use of solar thermal energy. *Energy*, 22(23):295–299, 1997. ISSN 0360-5442.

[63] P. A. Dellenback. Improved gas turbine efficiency through alternative regenerator configuration. volume 2A, pages 517–525, 2002.

[64] M. A. Habib, H. M. Badr, S. F. Ahmed, R. Ben-Mansour, K. Mezghani, S. Imashuku., G. J. la O', Y. Shao-Horn, N. D. Mancini, A. Mitsos, P. Kirchen, and A. F. Ghoneim. A review of recent developments in carbon capture utilizing oxy-fuel combustion in conventional and ion transport membrane systems. *International Journal of Energy Research*, 35(9):741–764, 2011. ISSN 1099-114X.

[65] R. Kehlhofer, F. Hannemann, F. Stirnimann, and B. Rukes. *Combined-Cycle Gas & Steam Turbine Power Plants.* PennWell Corporation, 3 edition, 2009.

[66] D. Mills. Advances in solar thermal electricity technology. *Solar Energy*, 76(13):19–31, 2004. ISSN 0038-092X.

[67] S. D. Odeh, M. Behnia, and G. L. Morrison. Performance evaluation of solar thermal electric generation systems. *Energy Conversion and Management*, 44(15):2425–2443, 2003. ISSN 0196-8904.

[68] S. A. Kalogirou. *Solar Energy Engineering: Processes and Systems.* Elsevier, 2009.

[69] F. Trieb, O. Langniß, and H. Klaiß. Solar electricity generation — A comparative view of technologies, costs and environmental impact. *Solar Energy*, 59(13):89–99, 1997. ISSN 0038-092X.

[70] R. Foster, M. D. Ghassemi, and A. Cota. *Solar Energy: Renewable Energy and the Environment.* CRC press, 2009.

[71] M. Eck, E. Zarza, M. Eickhoff, J. Rheinländer, and L. Valenzuela. Applied research concerning the direct steam generation in parabolic troughs. *Solar Energy*, 74(4):341–351, 2003. ISSN 0038-092X.

[72] J. A. Duffie and W. A. Beckman. *Solar Engineering of Thermal Processes.* John Wiley & Sons, 1991.